Earth, Planets and Space

FULL PAPER Open Access

Can the regional 3D stress field according to the Wallace–Bott hypothesis predict fault slip directions of future large earthquakes?

Takeo Ishibe[1,2*], Toshiko Terakawa[3], Akinori Hashima[4], Masashi Mochizuki[5] and Ritsuko S. Matsu'ura[1]

Abstract

When evaluating strong ground motions and tsunamis from specified source faults, it is required that the input parameters, such as fault geometry, rake angle, and slip amount, do not deviate from those of a real earthquake. Recently, a regional three-dimensional (3D) tectonic stress field was used to estimate rake angles for mapped submarine faults with the Wallace–Bott hypothesis (WBH), the direction of fault slip was parallel to the resolved stress vector on a preexisting fault, and strong ground motions and tsunamis were simulated. However, this modeling technique has not been adequately validated. Additionally, it is necessary to examine how the stress field estimated from seismological data for a limited period (~ 10 years) can be used as a proxy for the long-term tectonic stress field. In this study, to provide such validation, we utilized two catalogs of focal mechanism solutions for earthquakes and compared the observed rake angles with those calculated from the regional 3D tectonic stress field with the WBH by fixing the fault strike and dip angles according to those from the focal mechanism data. The resulting misfit angles between the observed and calculated rake angles are generally small (ranging between − 30° and 30°), excluding several regions (e.g., the source and surrounding regions of the 2011 off the Pacific coast of Tohoku earthquake and swarm-like activities activated after the 2011 quake). We also confirmed that the calculated rake angles and classified fault types are consistent with geomorphologically and geologically evaluated types of faulting for major Quaternary active faults in the Kyushu district of southwest Japan. These results support the validity and effectiveness of estimating rake angles for a specific fault with known geometry from the above method and data, while also showing that close attention is needed to apply this method to, for example, seismically inactive regions where the inverted stress field includes significant uncertainties and/or near sites of recent and large earthquakes where the stress field has been perturbed.

Keywords Wallace–Bott hypothesis, Tectonic stress field, Rake angles, F-net mechanism solutions, JUNEC FM[2], Quaternary active faults

*Correspondence:
Takeo Ishibe
ishibe@erc.adep.or.jp
Full list of author information is available at the end of the article

Graphical Abstract

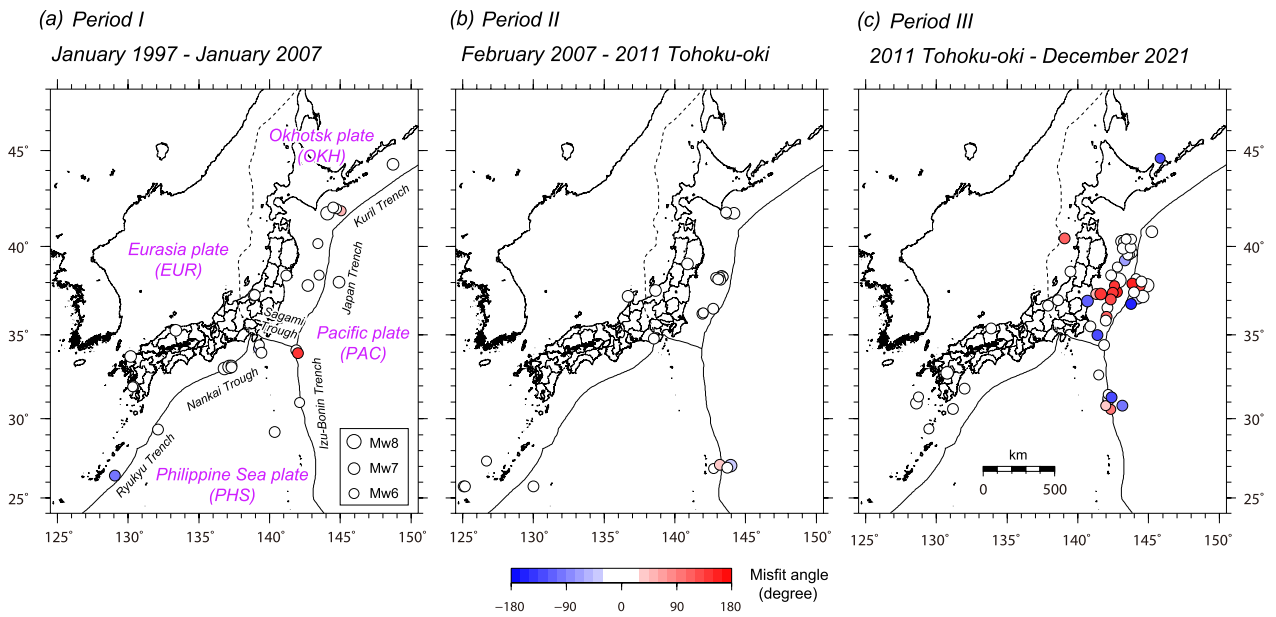

Introduction

In evaluating strong ground motions and tsunamis from a specified source fault, input parameters such as fault geometry (fault length, fault width, fault strike, and dip angle), rake angle, and slip amount are expected not to deviate from those for a future earthquake. Geometries of faults have been mainly investigated from geomorphological, geological, and seismological studies (e.g., aerial photo interpretation, trenching and coring surveys, seismic reflection and refraction surveys, and gravity anomalies). For expected slip amounts when the fault ruptures from known-geometry faults, empirical scaling relations between fault dimension (e.g., fault length, fault area) and slip amounts have been developed for various types of earthquakes (e.g., Wells and Coppersmith 1994; Takemura et al. 1998; Somerville et al. 1999; Irikura and Miyake 2001; Murotani et al. 2013, 2015). In contrast, the rake angle has been conventionally assumed to be a representative value for each fault type (i.e., 90° for reverse-fault type, −90° for normal fault type, 0° for left-lateral faults, and 180° for right-lateral faults), while setting rake angles is also essential for simulating strong ground motions and tsunamis. In particular, the appropriate setting is an indispensable issue for tsunami hazard assessment (e.g., Annaka et al. 2007; Mulia et al. 2020; Murotani et al. 2022; Satake et al. 2022).

The Japanese Islands are situated under a complicated tectonic setting due to the interaction of four major tectonic plates. The Pacific Plate subducts beneath the Okhotsk Plate along the Kuril and Japan Trenches and subducts beneath the Philippine Sea Plate along the Izu–Bonin Trench. Furthermore, the Philippine Sea Plate subducts beneath the Okhotsk Plate along the Sagami Trough and beneath the Eurasia Plate along the Suruga and Nankai Trough, and Ryukyu Trench. Resulting from this complicated tectonic setting, various types of faulting have occurred, and the resulting tectonic stress field has been investigated over the four past decades (e.g., Yoshii 1979; Huzita 1980; Wesnousky et al. 1982; Nishimura et al. 2004; Imanishi and Kuwahara 2009; Terakawa and Matsu'ura 2010; Matsushita and Imanishi 2015, Uchide et al. 2022).

Terakawa and Matsu'ura (2008) developed the CMT data inversion method to estimate the three-dimensional (3D) pattern of tectonic stress from the CMT data of seismic events by using Akaike's Bayesian Information Criterion (ABIC; Akaike et al. 1980). The essential difference between the CMT data inversion method and traditional stress inversion methods (e.g., Gephart and Forsyth 1984; Michael 1984, 1987) is the use of CMT data, which can be directly related to a tectonic stress field without any knowledge of actual physical processes in a source region and does not directly use the Wallace–Bott hypothesis (WBH; Wallace 1951; Bott 1959) (Fig. 1) to estimate the 3D tectonic stress field. Terakawa and Matsu'ura (2010) (TM2010) applied the CMT data inversion

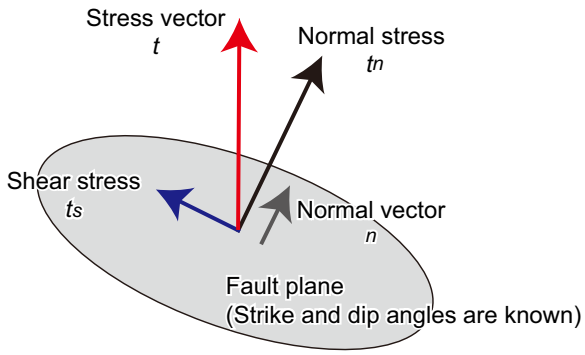

Fig. 1 Schematic illustration of the method for estimating rake angles from 3D tectonic stress fields with WBH

method to more than 12,500 moment tensor solutions ($3.0 \leq M \leq 5.0$) from January 1997 to January 2007 determined by using the Full Range Seismograph Network of Japan (F-net) and estimated the 3D tectonic stress field at depths ranging from 0 to 100 km in and around Japan (Fig. 2). In TM2010, each component of the 3D stress fields is represented by the superposition of 146,848 tricubic B splines with 20 and 10 km equally spaced grid intervals in the horizontal and vertical directions, respectively. This enables us to estimate six components of tectonic stress fields as continuous functions defined in the model region with estimation errors, although only relative values of six components have physical meaning. Figure 2 shows the spatial pattern of tectonic stress fields at a depth of 10 km. The stress pattern is represented with the lower hemisphere projections of focal spheres whose nodal planes indicate maximum shear stress planes. The colors of focal spheres indicate types of faulting according to the classification criteria by Frohlich (1992). TM2010 also verified that the estimated spatial pattern of stress field accorded with the focal mechanisms of large events ($M > 5.0$), which were not used for the CMT data inversion, and that they were well correlated with the present-day (Quaternary) tectonics of the Japanese islands.

Types and slip directions for inland faults have been mainly evaluated geologically and geomorphologically. Tectonic landforms due to a repetition of faulting include fault scarps and fault flexures for dip-slip faults and offsets for strike-slip faults. However, types and slip directions are not necessarily well known, especially those with low slip rates and/or those in regions with high erosion rates. Furthermore, landforms from strike-slip are usually less distinct than those from dip-slip, and types and slip directions are sometimes insignificant or controversial. Revealing fault types and slip directions for submarine faults generating tsunamis is further arduous due to limited data.

Recently, realistic rake angles for active submarine faults in Japan have been seismologically evaluated from 3D tectonic stress fields with WBH, and those rake angles were utilized for evaluating strong ground motions and tsunamis. For example, Research Committee on Large Earthquakes in the Sea of Japan (2014) and the Integrated Research Project on Seismic and Tsunami Hazards Around the Sea of Japan (Takeda et al. 2014) calculated rake angles expected from the 3D tectonic stress field by TM2010 with WBH, and then strong ground motions and tsunamis were simulated (e.g., Iwata et al. 2018; Satake et al. 2022).

However, the method of estimating rake angles from seismologically estimated stress fields with WBH has two outstanding issues. The first is that it has not been sufficiently validated. Because TM2010 did not directly use WBH, it is necessary to examine whether the tectonic stress field by TM2010 can reproduce the observed rake angles. The second is that the average recurrence interval of a characteristic earthquake in Japan generally ranges from tens to hundreds of years for events on a plate boundary (e.g., Ishibe and Shimazaki 2009) and several thousand years to tens of thousands of years for those on major Quaternary active faults (e.g., Ishibe and Shimazaki 2008, 2012). Considering that an earthquake releases the stress accumulated during those periods, it is necessary to examine whether the stress field estimated from seismological data for a limited period (~10 years) can be used as a proxy for the long-term tectonic stress fields.

In this study, we mainly focus on the first issue. As the first attempt at such verification, we compare rake angles for focal mechanism solutions of earthquakes from two catalogs: i.e., the F-net mechanism solutions (National Research Institute for Earth Science and Disaster Resilience 2023) and the Japan University Network Earthquake Catalog of First-Motion Focal Mechanisms (JUNEC FM^2; Ishibe et al. 2014), with rake angles expected from the 3D tectonic stress field with WBH. We also compare the geomorphologically and geologically evaluated fault types with those estimated from the tectonic stress field with WBH for major Quaternary active faults in the Kyushu district, southwest Japan, including the Futagawa and Hinagu fault zones (FZs) that were ruptured by the 2016 Kumamoto earthquake sequence.

Method and data

As part of this basic method to estimate stress fields, the WBH, in which the fault plane's slip direction is parallel to the direction of shear traction on the fault plane, has been widely utilized (Fig. 1). Given a stress tensor $\boldsymbol{\sigma}$, the traction vector at the fault plane whose normal vector is $\mathbf{n}$ can be described by the following equation:

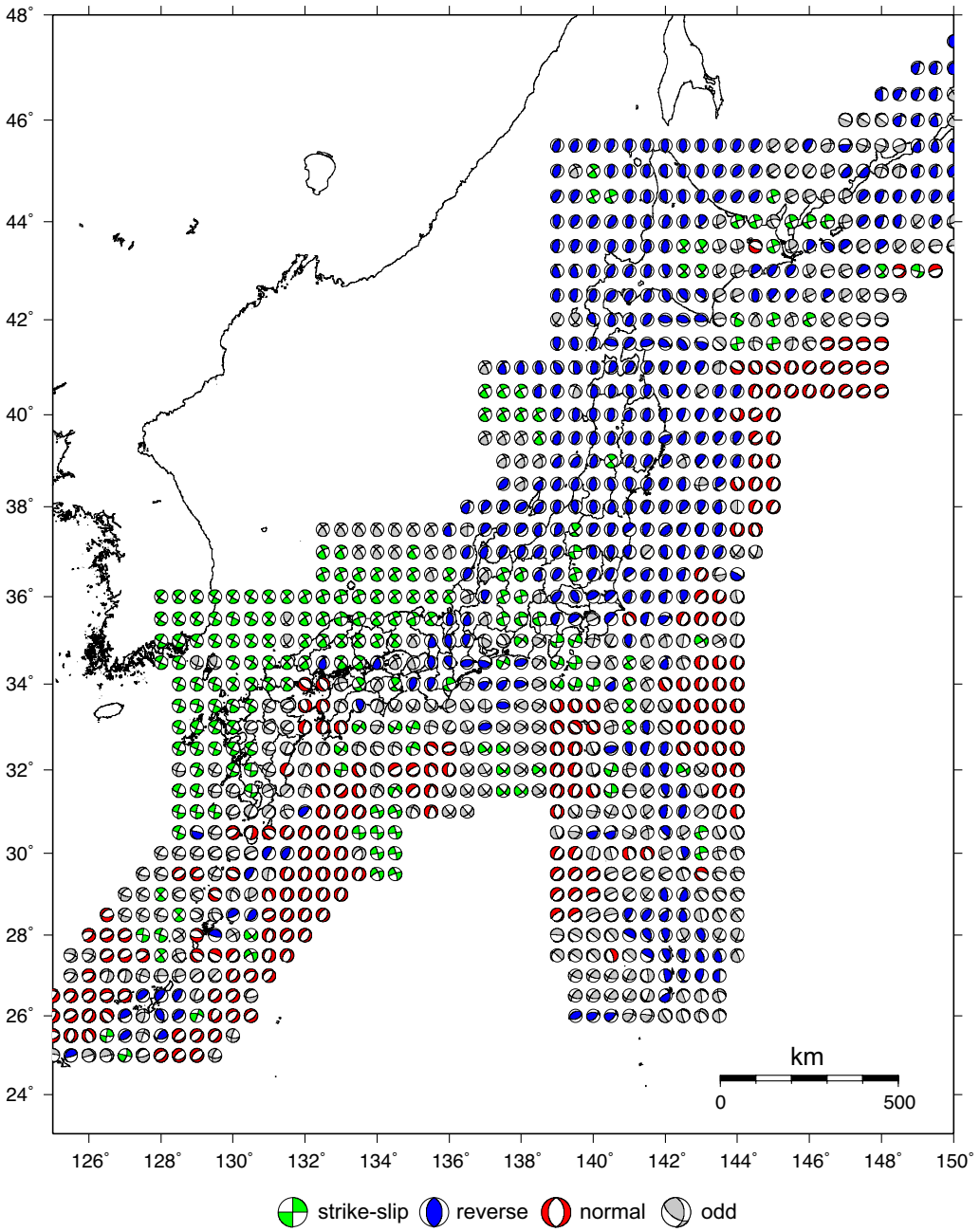

Fig. 2 The stress pattern at 10 km in depth after Terakawa and Matsu'ura (2010). The stress pattern is represented by the lower hemisphere projection of focal mechanisms of potential seismic events. The colors indicate types of faulting according to the classification criteria by Frohlich (1992)

$$\mathbf{t} = \boldsymbol{\sigma}\mathbf{n}.$$

The normal and tangential components of this vector are the normal and shear traction vectors and are given by:

$$\mathbf{t_n} = (\mathbf{n}\cdot\mathbf{t})\mathbf{n} = [\mathbf{n}\cdot(\boldsymbol{\sigma}\mathbf{n})]\mathbf{n},$$

$$\mathbf{t_s} = \mathbf{t} - \mathbf{t_n} = \boldsymbol{\sigma}\mathbf{n} - [\mathbf{n}\cdot(\boldsymbol{\sigma}\mathbf{n})].$$

Fault slip occurs to release the shear stress, and hence, the theoretical slip direction can be described by the unit vector $\mathbf{t_s}/|t_s|$, where $|t_s|$ is the length of the shear traction vectors. The rake angles can be obtained

by taking angles between the fault slip direction and fault strike.

The National Research Institute for Earth Science and Disaster Resilience (NIED) began to install a nationwide broadband seismograph network in 1994 under the Fundamental Research on Earthquakes and Earth's Interior Anomaly (FREESIA) project, and after the project terminated in March 2001, the seismograph network was integrated into the network installed as a part of the measure by the Headquarter for Earthquake Research Promotion (HERP) as F-net (Okada et al. 2004).

In the present study, we validate the method of estimating rake angles from the 3D tectonic stress field obtained by TM2010 with WBH for F-net data spanning from January 1997 to December 2021 with the centroid ranging from 125° to 150° E in longitude and 25°–47° N in latitude. To validate the applicability of the method to Quaternary active faults in the shallow crust, we utilize all available focal mechanism solutions of earthquakes with a centroid depth of 30 km or shallower regardless of their variance reductions (VR). The number of validated F-net mechanism solutions is 20,148 with moment magnitudes (M_w) ranging from 3.1 to 8.7. We fix the strike and dip angles of the fault to nodal planes of the focal mechanism solutions and calculate (theoretical) rake angles expected from the 3D tectonic stress field by TM2010 with WBH (hereafter referred to as calculated rake angles). The calculated rake angles are then compared with the actual rake angles of focal mechanisms for earthquakes (hereafter referred to as observed rake angles) by calculating misfit angles. The misfit angles (hereafter, denoted by λ) are defined by the O (observed rake angles by the F-net) − C (calculated rake angles). Here, the smaller absolute misfit angle (hereafter denoted by $|\lambda|$) between the first and second nodal planes is adopted as a representative value. We separate the period of the F-net mechanism data into three intervals (Fig. 3): from January 1997 to January 2007 (Period I), from February 2007 to the occurrence of the 2011 off the Pacific coast of Tohoku earthquake (M_{JMA}9.0 [magnitude determined by the Japan Meteorological Agency (JMA)], M_w8.7 [F-net]; hereafter referred to as the 2011 Tohoku-oki earthquake) (Period II), and the postseismic period of the 2011 Tohoku-oki earthquake (Period III). We set Period I to confirm the applicability of the method because TM2010 does not directly use WBH to invert the 3D tectonic stress field. We further divide the latter period into two periods at the occurrence of the 2011 Tohoku-oki earthquake on March 11 because significant changes in seismicity were reported following the 2011 event (e.g., Hirose et al. 2011; Ishibe et al. 2011a, 2015, 2017; Toda et al. 2011). The numbers of validated focal mechanisms are 6191, 2623, and 11,334 for Period I, Period II, and Period III, respectively.

We also utilize JUNEC FM^2 (Ishibe et al. 2014; Additional file 1: Fig. S1) for validation. JUNEC FM^2 contains focal mechanism solutions for 14,544 earthquakes that occurred in and around the Japanese Islands from July 1985 to December 1998. This catalog was determined by using first-motion polarities reported by the Japan University Seismic Network and covers small-magnitude earthquakes ($M \geq 2.0$) prior to the recent development of seismic observation networks and automated waveform data processing systems. We validate the method for 7221 focal mechanism solutions of earthquakes with qualities of "A", "B", or "C", epicenters ranging from 125° to 150° E in longitude and 25°–47° N in latitude, and depths of 30 km or shallower. All results for JUNEC FM^2 are shown in the supplementary materials (Additional file 1: Fig. S1, Additional file 2: Fig. S2, Additional file 3: Fig. S3, Additional file 4: Fig. S4).

In Japan, the HERP has selected 114 (as of November 2023) major active FZs as basic survey targets, considering the degree of activity and the impact on society when the fault ruptures, to efficiently survey many active faults. HERP also compiled the outcomes of previous surveys, evaluated fault geometry (fault length, width, dip angle, fault strike), fault type, histories of past activities, and average recurrence intervals, and then conducted long-term evaluations (e.g., expected earthquake magnitude, earthquake occurrence probability during the next 30 years) (e.g., HERP 2013). To investigate whether the above geomorphologically and geologically evaluated fault types can be reproduced from the 3D tectonic stress field with WBH, we compare geomorphologically and geologically evaluated fault types with calculated rake angles for major Quaternary active faults in the Kyushu district, southwest Japan. Along the Futagawa and Hinagu FZs in the central part of the Kyushu district, large earthquakes called the 2016 Kumamoto earthquake sequence occurred in April 2016 and caused severe damage near the source region (e.g., Yamada et al. 2017). We use the fault types evaluated by HERP and the fault models obtained from the Japan Seismic Hazard Information Station (J-SHIS) by NIED. We calculate the rake angles at the center of each fault and classify these faults as reverse-fault type (rake angle: 90° ± 45°), normal fault type (rake angle: −90° ± 45°), left-lateral fault (rake angle: 0° ± 45°), and right-lateral fault (rake angle: 180° ± 45°). These fault types are then compared with geomorphologically and geologically estimated fault types.

Validation of the method for the F-net focal mechanism catalog

Period I (January 1997–January 2007)

During Period I, in which the moment tensor solutions of earthquakes were used for the CMT data inversion by

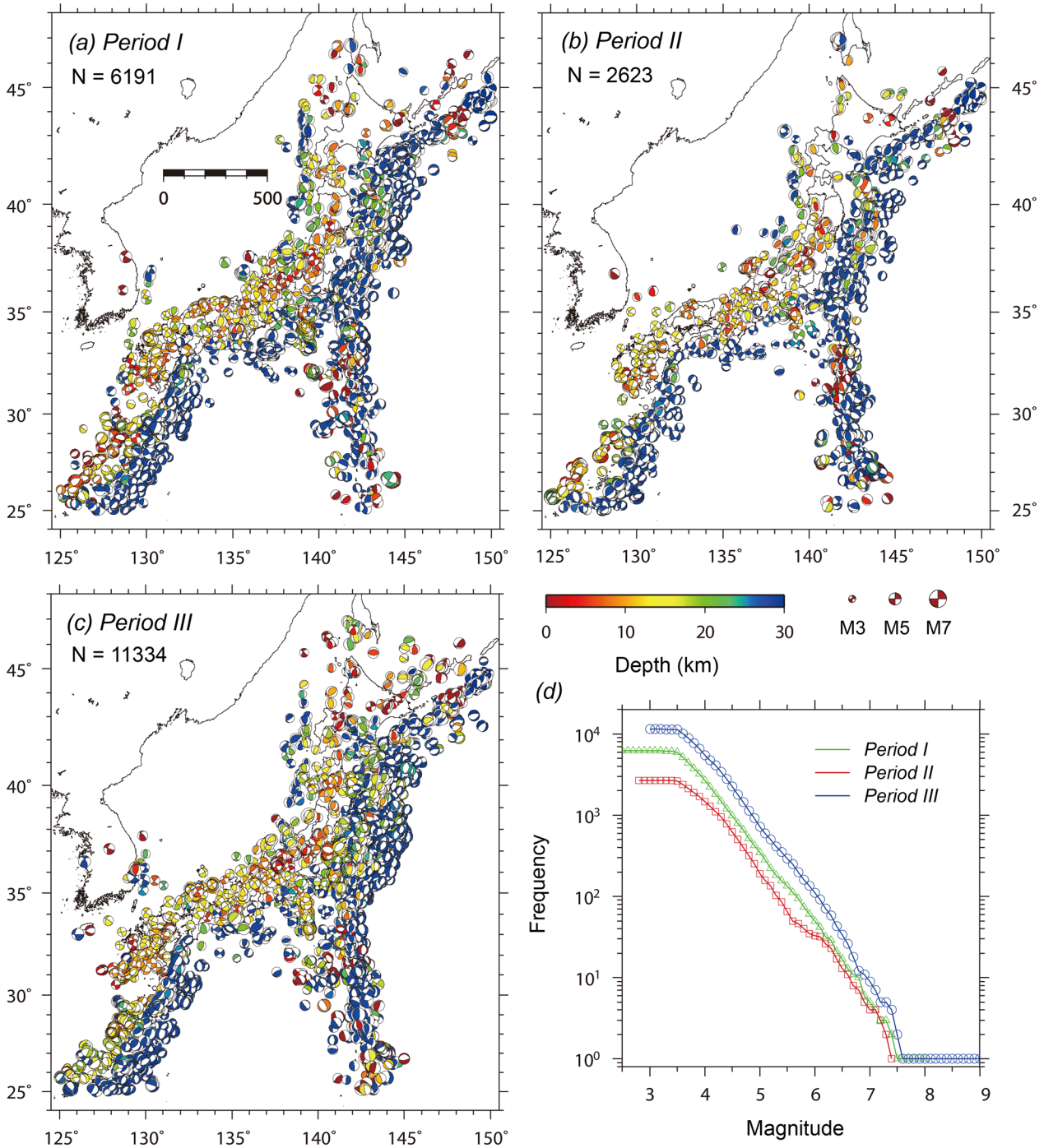

Fig. 3 Distribution of focal mechanism solutions (centroid depth ≤ 30 km) used for the validation for **a** Period I (January 1997 to January 2007), **b** Period II (February 2007 to the occurrence time of the 2011 Tohoku-oki earthquake), and **c** Period III (postseismic period of the 2011 Tohoku-oki earthquake). The colors indicate centroid depth. **d** Magnitude frequency distribution of earthquakes for each period

TM2010, the calculated rake angles are mostly consistent with the observed rake angles (Figs. 4 and 5). Misfit angles λ mostly range between $-30°$ and $30°$ with an average of $-1.81°$ and a standard deviation of $20.78°$. The histogram of λ shows a clear Gaussian distribution with a center of approximately zero. Among 6191 earthquakes, $|\lambda|$ is $\leq 30°$ (class A) for 5846 (~94.4%) earthquakes, whereas 204 (~3.3%), 34 (~0.5%) and 107 (~1.7%)

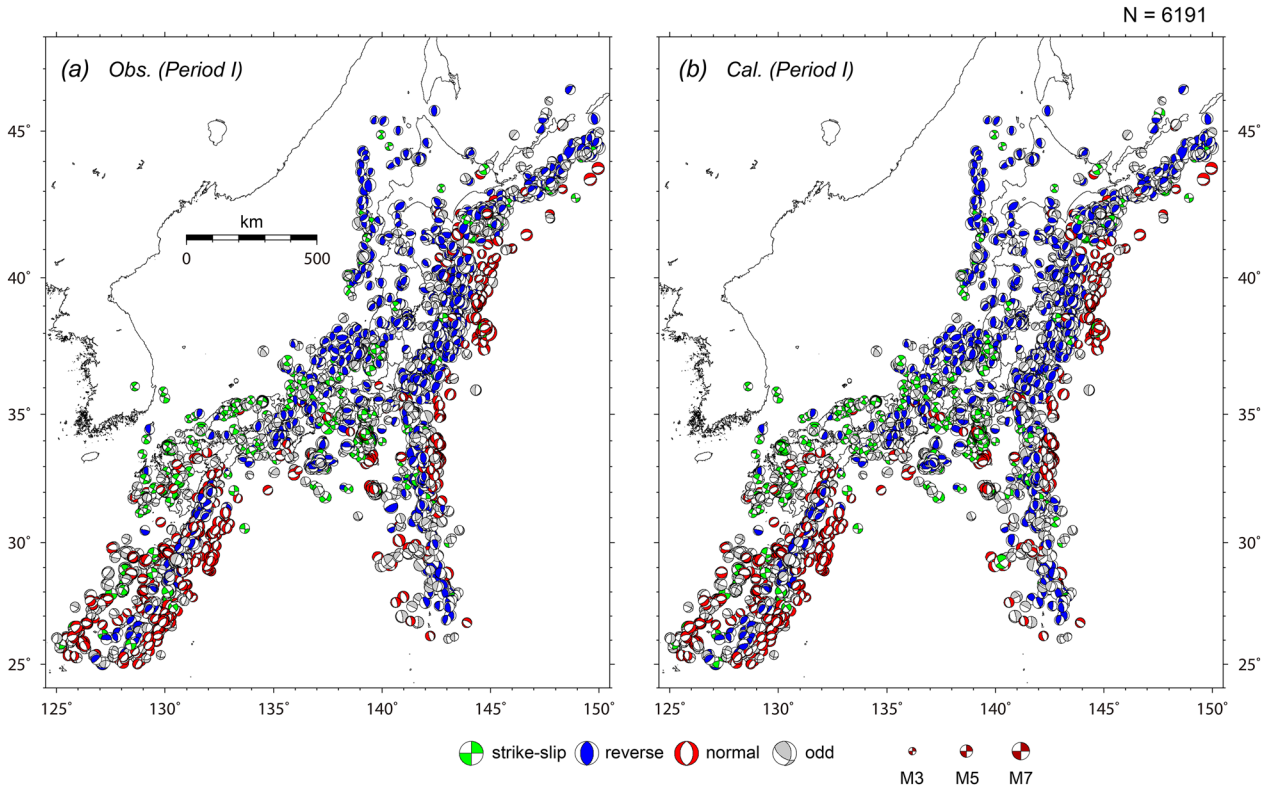

Fig. 4 **a** Distribution of F-net focal mechanism solutions of earthquakes that occurred in Period I. **b** Distribution of focal mechanism solutions with calculated rake angles from the 3D tectonic stress fields with WBH for Period I. The colors indicate fault types according to the classification criteria by Frohlich (1992)

earthquakes exhibit $30° < |\lambda| \leq 60°$ (class B), $60° < |\lambda| \leq 90°$ (class C) and $|\lambda| > 90°$ (class D), respectively (Fig. 6). Earthquakes with large $|\lambda|$ are concentrated in subduction zones and aftershock regions following large (M_w6.0 or above) earthquakes, such as the M_w7.9 interplate earthquake that occurred along the Kuril Trench on 26th September 2003 in southeastern off Tokachi (called the 2003 Tokachi-oki earthquake by JMA) (No. 13 in Fig. 7a and Table 1), while $|\lambda|$ is mostly small for the mainshock as discussed in the next paragraph. The close-up figures of the comparison of the calculated rake angles with the observed rake angles in Hokkaido (Additional file 5: Fig. S5, Additional file 6: Fig. S6, Additional file 7: Fig. S7), Tohoku (Additional file 8: Fig. S8, Additional file 9: Fig. S9, Additional file 10: Fig. S10), Kanto and Chubu (Additional file 11: Fig. S11, Additional file 12: Fig. S12, Additional file 13: Fig. S13), Chugoku and Shikoku (Additional file 14: Fig. S14, Additional file 15: Fig. S15, Additional file 16: Fig. S16), and Kyushu (Additional file 17: Fig. S17, Additional file 18: Fig. S18, Additional file 19: Fig. S19) districts, Ryukyu Trench region (Additional file 20: Fig. S20, Additional file 21: Fig. S21, Additional file 22: Fig. S22) and Izu–Bonin Trench region (Additional file 23: Fig. S23, Additional file 24: Fig. S24, Additional file 25: Fig. S25) for each period are shown in Additional files. The basic characteristics of faulting [i.e., the reverse faulting dominantly distributed in northeastern Japan (Additional file 9: Fig. S9), the mixture of reverse faulting and strike-slip faulting in central Japan (Additional file 12: Fig. S12), and strike-slip faulting and normal faulting in southwestern Japan (Additional file 15: Fig. S15 and Additional file 18: Fig. S18)] are well reproduced from the 3D tectonic stress field with WBH.

The $|\lambda|$ values are also small for large (M_w6.0 or above) earthquakes. Among 29 earthquakes with M_w6.0 or above during Period I, $|\lambda|$ is smaller than 20° for 24 (~82.8%) earthquakes and smaller than 30° for 25 (~86.2%) earthquakes (Table 1). For example, the calculated rake angle is 82.58° and λ is 4.42° for a reverse-type M_w6.1 earthquake that occurred on 26th July 2003 in northern Miyagi Prefecture (No. 12 in Fig. 7a and Table 1). The observed rake angle of the M_w6.6 earthquake that occurred on 20th March 2005 in the southwestern off Kyushu district (−177°; named the 2005 Fukuoka-ken Seiho-oki earthquake by JMA) can also be well reproduced by the method (169.49°) with $\lambda = 13.51°$ (No. 26 in Fig. 7a and Table 1). Furthermore, the M_w7.9 interplate earthquake that occurred along the Kuril Trench on 26th

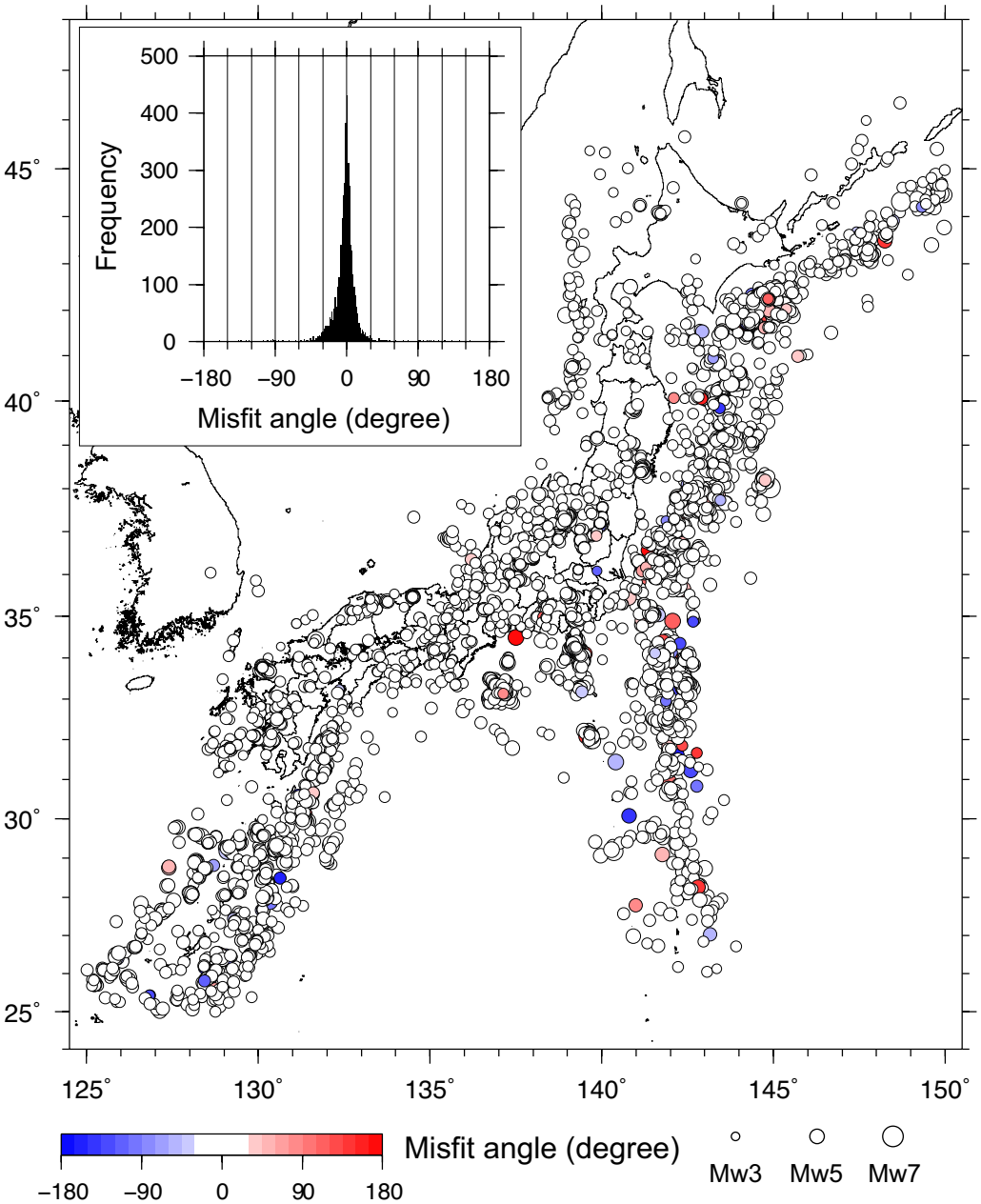

Fig. 5 Distribution of λ between the observed and calculated rake angles during Period I

September 2003 in southeastern off Tokachi (called the 2003 Tokachi-oki earthquake by JMA) is well reproduced by the method with $\lambda = 8.01°$ (No. 13 in Fig. 7a and Table 1). On the other hand, four earthquakes exhibit $|\lambda| > 30°$ (Fig. 7a). A typical example is the M_w6.5 earthquake, which occurred on 19th January 2005 in the far southeastern off Boso Peninsula near the triple junction among the Pacific, Philippine, and Okhotsk plates (No. 25 in Fig. 7a and Table 1). The observed focal mechanism solution for this earthquake is a reverse-type with a rake angle of 105°, whereas the calculated one is a left-lateral with a normal-faulting component, and the resulting λ is 142.90°. The possible causes of the relatively large $|\lambda|$ for these earthquakes are discussed in the next chapter.

Period II (February 2007—the 2011 Tohoku-oki earthquake)

Similarly, the calculated rake angles are mostly consistent with the observed rake angles for Period II (Figs. 8 and 9). $|\lambda|$ values are also mostly $\leq 30°$ and the histogram of

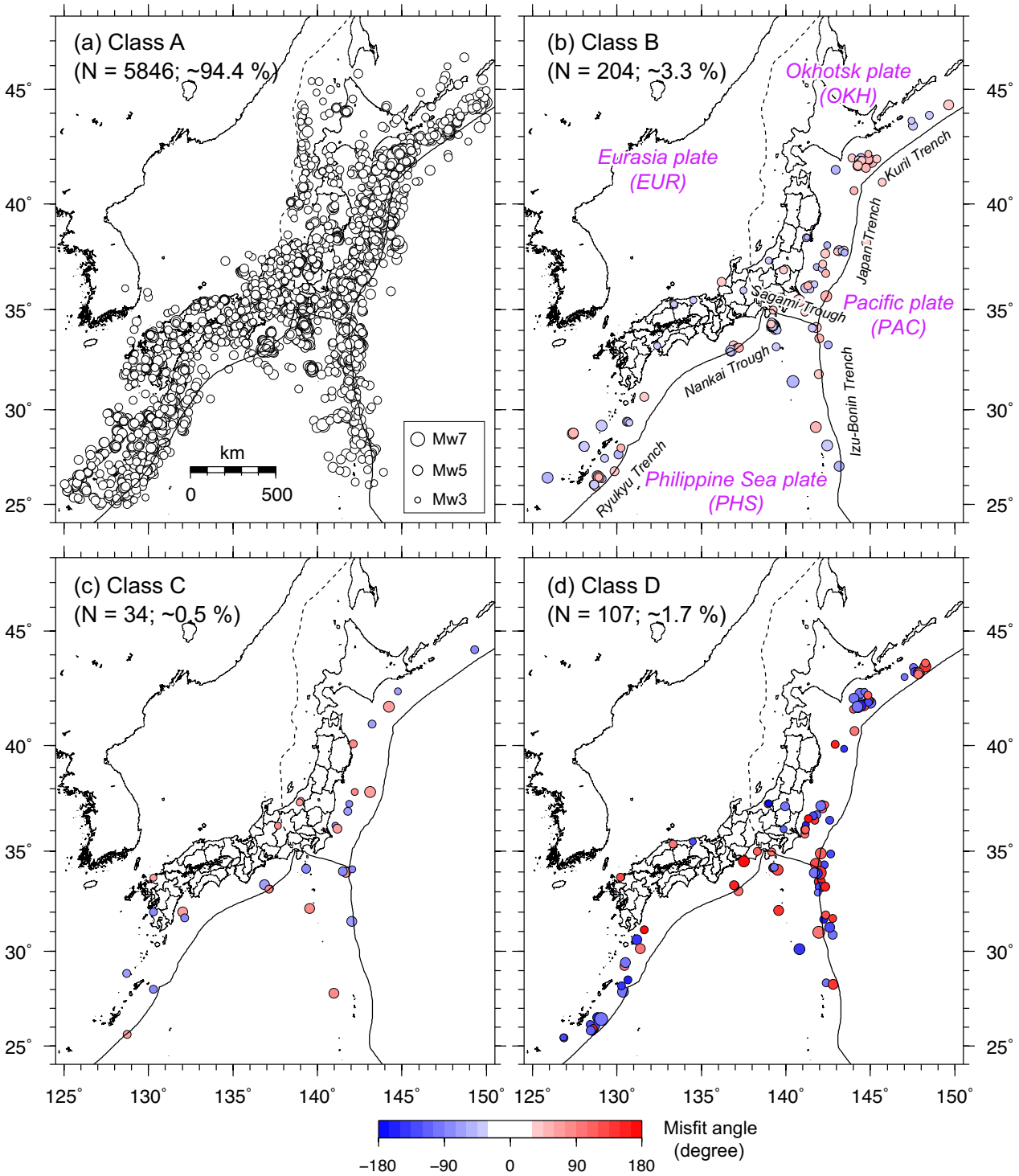

Fig. 6 Distribution of λ between the observed and calculated rake angles during Period I for **a** class A ($|\lambda| \leq 30°$), **b** class B ($30° < |\lambda| \leq 60°$), **c** class C ($60° < |\lambda| \leq 90°$) and **d** class D ($|\lambda| > 90°$)

λ shows a clear Gaussian distribution with an average of $-2.93°$ and a standard deviation of 50.01°. The basic characteristics of faulting in Japan are also well reproduced from the 3D tectonic stress field with WBH. Among the 2623 earthquakes, $|\lambda|$ is classified as class A for 1970 (~75.1%) earthquakes, whereas 237 (~9.0%), 97 (~3.7%)

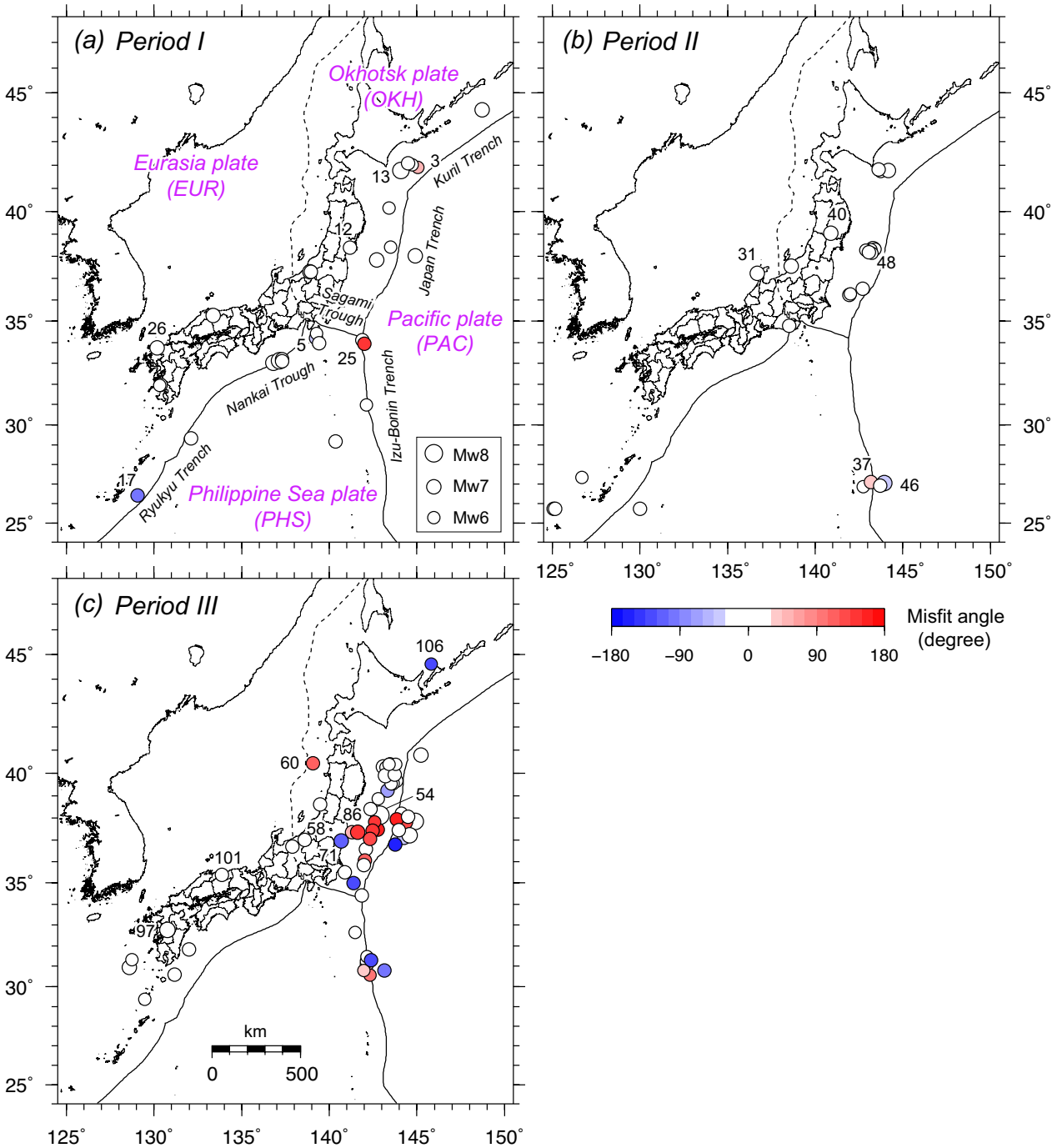

Fig. 7 Distribution of λ for large ($M_w \geq 6.0$) earthquakes that occurred during **a** Period I, **b** Period II, and **c** Period III. The numbers in the figures are the IDs in Tables 1, 2, 3

and 319 (~12.2%) earthquakes are classified as classes B, C and D, respectively (Fig. 10). The larger standard deviation results from several regions where the relatively large $|\lambda|$ values are concentrated, i.e., along the Izu–Bonin Trench and Ryukyu Trench (Fig. 9). Furthermore, aftershocks in the source and nearby regions of major earthquakes exhibit relatively large $|\lambda|$ values, such as the 2007 Noto Hanto earthquake and 2008 Iwate-Miyagi Nairiku earthquake, while the mainshock is well reproduced by the method as described below.

Table 1 List of focal mechanism solutions for large ($M_w \geq 6.0$) earthquakes with calculated rake angles and λ during Period I

No.	Year	Month	Day	Hour	Minute	Second	Longitude (deg.)	Latitude (deg.)	Depth (km)	M_w	Strike (deg.)	Dip angle (deg.)	Rake angle (deg.)	Region	Variance reduction (%)	Calculated rake angle (deg.)	Misfit angle (deg.)
1	1997	3	26	17	31	47.90	130.3613	31.9693	8	6.1	103	88	−9	NW_KAGOSHIMA_PREF	91.17	−7.27	−1.73
2	1997	5	13	14	38	27.59	130.3050	31.9448	11	6.0	191	88	−175	NW_KAGOSHIMA_PREF	95.30	175.48	9.52
3	1997	10	9	6	20	57.88	145.0528	41.8923	8	6.0	201	85	75	SE_OFF_TOKACHI	83.24	27.82	47.18
4	2000	6	15	20	10	48.51	132.1110	29.3328	11	6.1	180	18	−103	N_PHILIPPINE_BASIN	92.69	−100.98	−2.02
5	2000	7	1	16	1	56.72	139.2217	34.2053	5	6.2	352	75	−52	NEAR_NIIJIMA_ISLAND	90.67	−20.83	−31.17
6	2000	7	15	10	30	32.30	139.2533	34.4235	8	6.0	16	78	−8	NEAR_NIIJIMA_ISLAND	92.76	−11.78	3.78
7	2000	7	30	21	25	46.58	139.4002	33.9617	11	6.4	11	85	−13	NEAR_MIYAKEJIMA_ISLAND	90.42	−19.48	6.48
8	2000	10	3	13	13	28.21	143.3983	40.1547	26	6.0	195	31	78	FAR_E_OFF_SANRIKU	86.09	75.51	2.49
9	2000	10	6	13	30	18.03	133.3498	35.2752	11	6.6	150	85	−9	WESTERN_TOTTORI_PREF	92.18	−9.29	0.29
10	2001	5	25	9	40	54.17	148.7072	44.3185	23	6.6	227	25	108	SE_OFF_ETOROFU	80.79	114.74	−6.74
11	2002	8	20	19	59	32.68	142.1067	30.9912	5	6.0	198	39	114	NEAR_TORISHIMA_IS	89.30	106.57	7.43
12	2003	7	26	7	13	31.52	141.1745	38.4020	5	6.1	186	52	87	NORTHERN_MIYAGI_PREF	88.48	82.58	4.42
13	2003	9	26	4	50	7.64	144.0785	41.7797	23	7.9	31	78	81	SE_OFF_TOKACHI	87.14	72.99	8.01
14	2003	9	27	5	38	22.31	144.7320	42.0232	26	6.0	262	36	156	SE_OFF_TOKACHI	86.13	151.81	4.19
15	2003	10	31	10	6	30.67	142.6995	37.8292	26	6.7	27	64	95	SE_OFF_MIYAGI_PREF	93.26	94.46	0.54
16	2004	5	30	5	56	6.04	141.8623	34.1045	5	6.2	169	25	43	FAR_SE_OFF_BOSO_PEN	52.15	45.02	−2.02
17	2004	7	22	18	45	13.37	129.0357	26.4382	23	6.1	71	59	−12	NEAR_OKINAWAJIMA_ISLAND	80.53	92.77	−104.77

Table 1 (continued)

No.	Year	Month	Day	Hour	Minute	Second	Longitude (deg.)	Latitude (deg.)	Depth (km)	M_w	Strike (deg.)	Dip angle (deg.)	Rake angle (deg.)	Region	Variance reduction (%)	Calculated rake angle (deg.)	Misfit angle (deg.)
18	2004	9	5	19	7	7.50	136.8005	33.0297	14	7.2	86	38	89	SE_OFF_KII_PENINSULA	91.37	89.82	−0.82
19	2004	9	5	23	57	16.93	137.1423	33.1435	11	7.5	245	62	62	SE_OFF_KII_PENINSULA	91.01	60.08	1.92
20	2004	9	7	8	29	36.27	137.2958	33.2057	11	6.5	74	42	61	SE_OFF_KII_PENINSULA	77.40	72.69	−11.69
21	2004	9	8	23	58	23.16	137.2905	33.1143	5	6.1	239	37	54	SE_OFF_KII_PENINSULA	75.68	82.29	−28.29
22	2004	10	23	17	56	0.30	138.8703	37.2895	5	6.6	27	43	87	MID_NIIGATA_PREF	88.13	92.36	−5.36
23	2004	10	23	18	34	5.69	138.9332	37.3033	11	6.3	221	59	94	MID_NIIGATA_PREF	84.43	94.93	−0.93
24	2004	11	11	19	2	46.17	144.4895	42.0777	29	6.1	264	36	158	SE_OFF_TOKACHI	87.64	158.23	−0.23
25	2005	1	19	15	11	30.30	141.9928	33.9525	11	6.5	7	48	105	FAR_SE_OFF_BOSO_PEN	93.54	−37.90	142.90
26	2005	3	20	10	53	40.32	130.1763	33.7392	11	6.6	213	79	−177	NW_OFF_KYUSHU	95.47	169.49	13.51
27	2005	8	31	3	10	40.29	143.4805	38.4115	23	6.0	232	38	116	FAR_E_OFF_MIYAGI_PREF	90.91	114.37	1.63
28	2005	11	15	6	38	52.08	144.8895	38.0305	14	7.0	178	63	−105	FAR_E_OFF_NORTH_HONSHU	93.86	−108.51	3.51
29	2006	10	24	6	17	16.94	140.3513	29.1742	5	6.4	318	56	−99	NEAR_TORISHIMA_IS	77.11	−98.15	−0.85

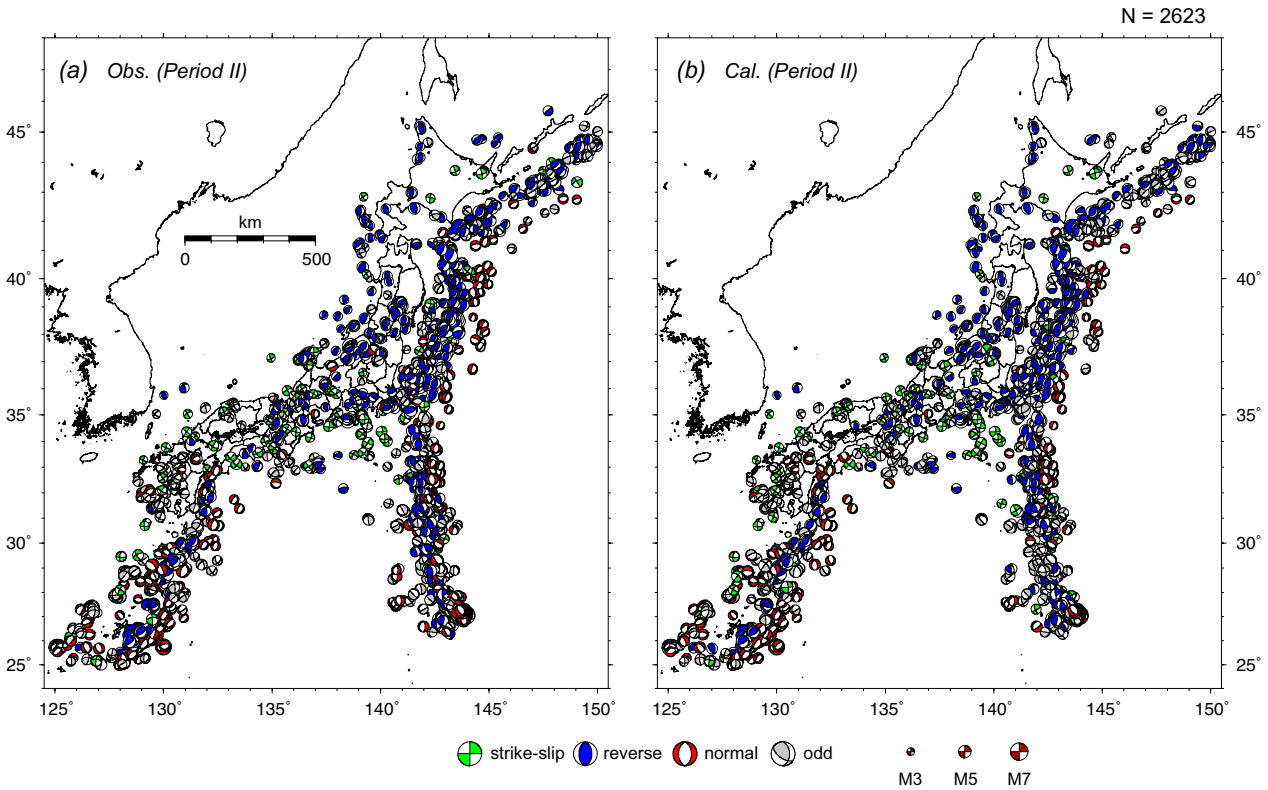

Fig. 8 **a** Distribution of F-net focal mechanism solutions of earthquakes that occurred in Period II. **b** Distribution of focal mechanism solutions with calculated rake angles from the 3D tectonic stress fields with WBH for Period II. The colors indicate fault types according to the classification criteria by Frohlich (1992)

Among the 24 earthquakes with M_w6.0 or above that occurred during Period II, $|\lambda|$ is $\leq 20°$ for 20 (~83.3%) earthquakes and $\leq 30°$ for 22 (~91.7%) earthquakes (Table 2; Fig. 7b). The rake angles for major inland shallow earthquakes such as the 2007 Noto Hanto earthquake (M_w6.7) that occurred on 25th March ($\lambda = -5.58°$, No. 31 in Fig. 7b and Table 2) and the 2008 Iwate-Miyagi Nairiku earthquake (M_w6.9) that occurred on 14th June ($\lambda = 6.28°$, No. 40 in Fig. 7b and Table 2) are well reproduced by the 3D tectonic stress field with WBH. Furthermore, observed rake angles for great interplate earthquakes that occurred during Period II, such as the M_w7.2 earthquake that occurred east off Miyagi Prefecture on 9th March, 2 days before the 2011 Tohoku-oki earthquake ($\lambda = -4.53°$, No. 48 in Fig. 7b and Table 2), are also reproduced by the method. On the other hand, only two earthquakes exhibit $|\lambda| > 30°$. Both earthquakes occurred near Chichi-jima Island along the Izu–Bonin Trench. One is the M_w6.2 earthquake (No. 37 in Fig. 7b and Table 2) with $\lambda = 41.58°$, which occurred on 15th March 2008, and the other is the M_w7.3 earthquake (No. 46 in Fig. 7b and Table 2) with $\lambda = -38.03°$, which occurred on 22nd December 2010. Similar to the result for Period I, these earthquakes occurred far offshore, where the observation stations are sparse.

Period III (2011 Tohoku-oki earthquake—December 2020)

During Period III, the calculated rake angles are essentially consistent with the observed rake angles with $|\lambda| \leq 30°$ (Figs. 7c, 11, 12, 13; Table 3) except for the source and neighboring regions of the major earthquakes (i.e., the 2011 Tohoku-oki earthquake). Among the 11,334 earthquakes, $|\lambda|$ is classified as class A for 6490 (~57.3%) earthquakes, whereas 910 (~8.0%), 541 (~4.8%) and 3393 (~29.9%) earthquakes are classified as classes B, C and D, respectively (Fig. 13). For example, the rake angle of the 2011 Tohoku-oki earthquake could be well reproduced by the method with $\lambda = -7.01°$ (No. 54 in Fig. 7c and Table 3), while $|\lambda|$ is slightly larger ($\lambda = 8.68°$) for the thrust-type (actual) nodal plane. In addition, the rake angles of crustal earthquakes such as the 2016 Kumamoto earthquake (M_w7.1) that occurred on 16th April ($\lambda = -0.20°$, No. 97 in Fig. 7c and Table 3) and the 2016 Tottori-ken Chubu earthquake (M_w6.2) that occurred on 21st October ($\lambda = -6.96°$, No. 101 in Fig. 7c and Table 3) were also consistent with the observed values. The M_w6.2

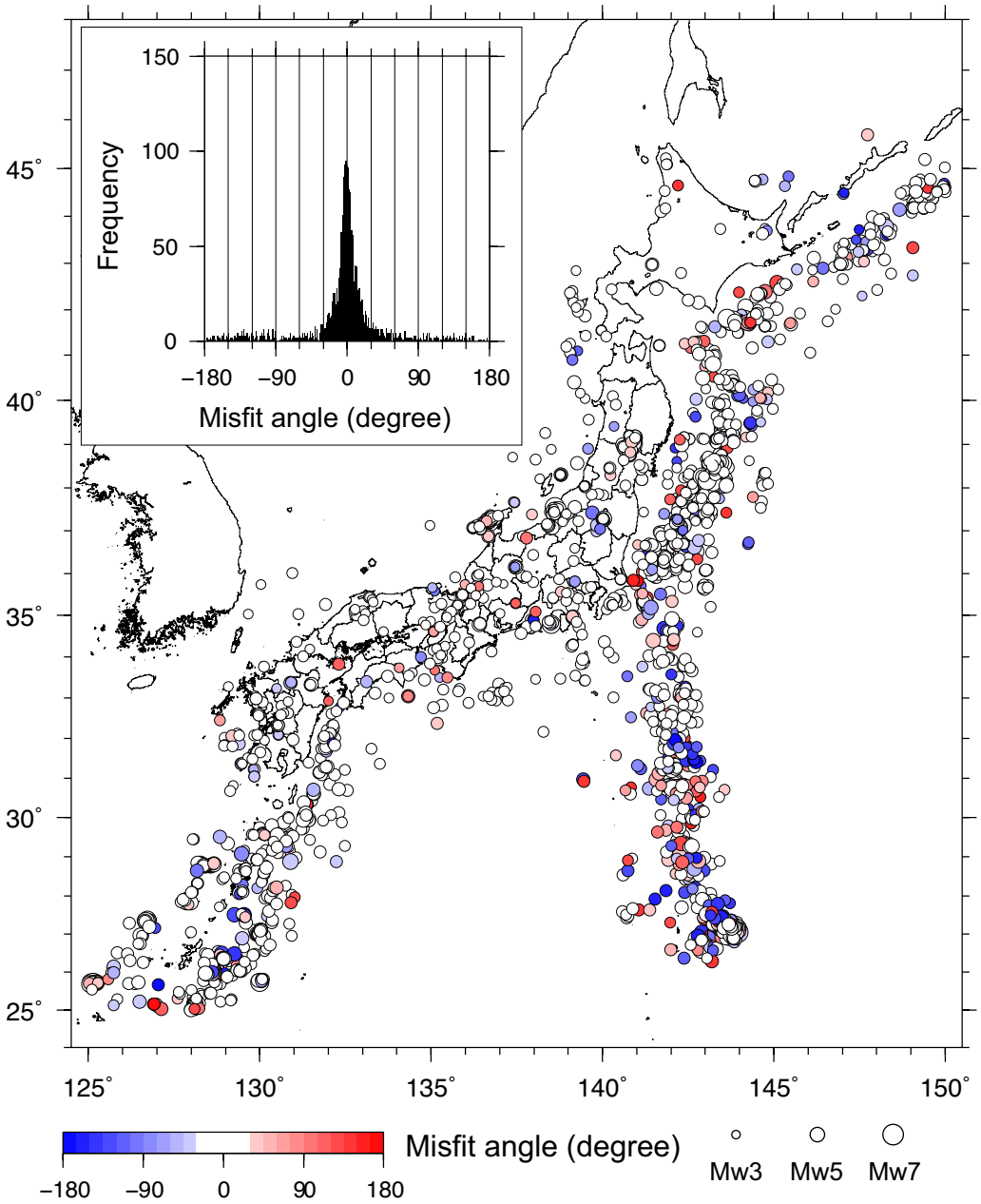

Fig. 9 Distribution of λ between the observed and calculated rake angles during Period II

earthquake in the mid-Niigata Prefecture on 12th March 2011, possibly remotely triggered by the 2011 Tohoku-oki earthquake, exhibits consistent a rake angle with the observed rake angle ($\lambda = 3.82°$, No. 58 in Fig. 7c and Table 3), whereas the M_w6.1 earthquake that occurred west-off Aomori Prefecture on 12th March 2011 (the same day as the M_w6.2 earthquake in the mid-Niigata Prefecture) exhibits a large $|\lambda|$ ($\lambda = 111.44°$, No. 60 in Fig. 7c and Table 3).

The earthquakes that occurred in the source and neighboring regions of the major earthquakes (i.e., the 2011 Tohoku-oki earthquake) particularly showed large $|\lambda|$. One representative example showing large $|\lambda|$ values is an earthquake sequence in the prefectural boundary region between Ibaraki and Fukushima, where normal faulting earthquakes abruptly began to occur following the 2011 Tohoku-oki earthquake (Fig. 14; e.g., Kato et al. 2011). The largest shock in the sequence was the M_w6.6 Fukushima Hama-Dori earthquake ($\lambda = -116.30°$, No. 71

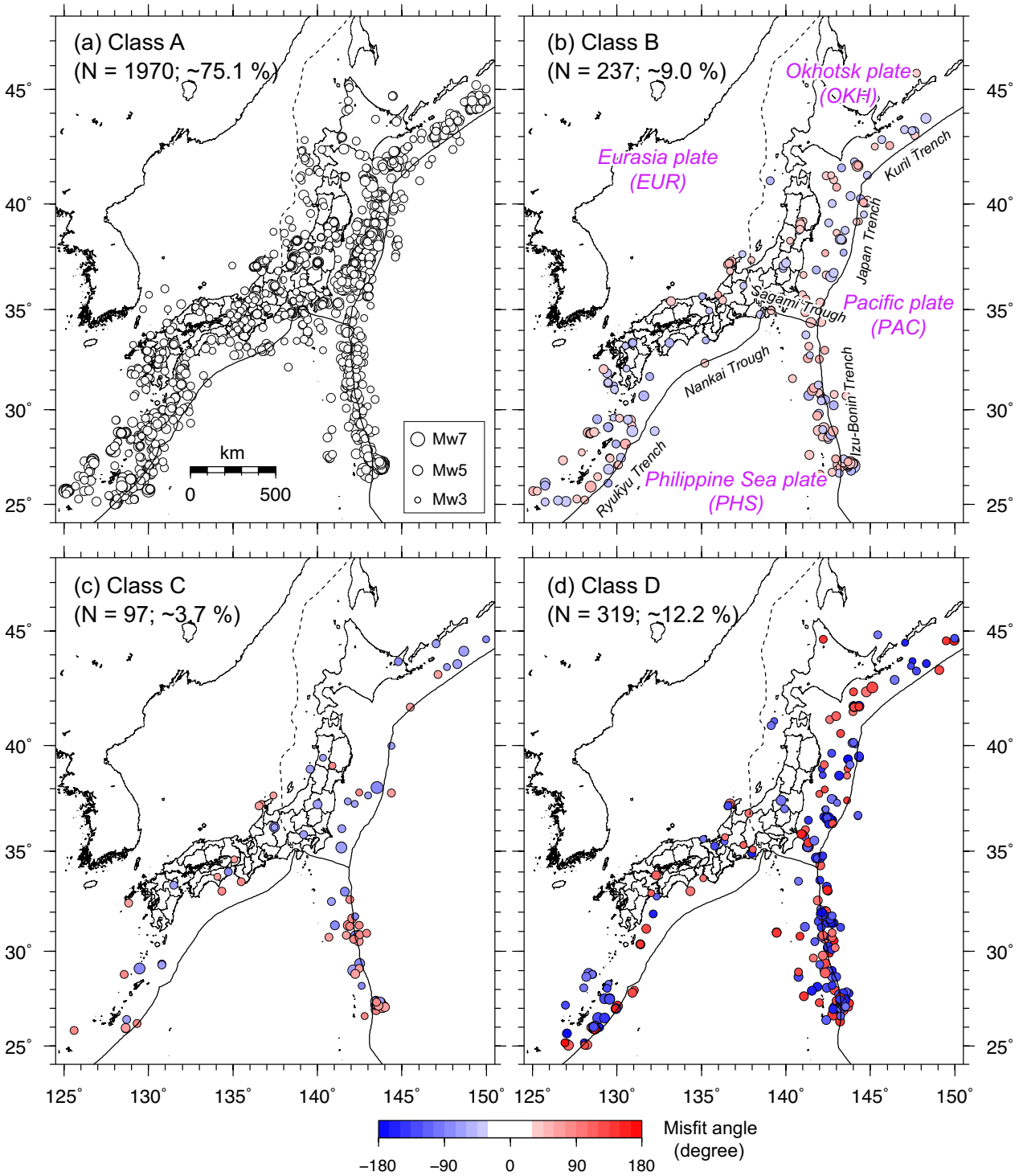

Fig. 10 Distribution of λ between the observed and calculated rake angles during Period II for **a** class A ($|\lambda| \leq 30°$), **b** class B ($30° < |\lambda| \leq 60°$), **c** class C ($60° < |\lambda| \leq 90°$) and **d** class D ($|\lambda| > 90°$)

in Fig. 7c and Table 3), occurred 1 month after the 2011 Tohoku-oki earthquake. The $|\lambda|$ values for this sequence are enormously large because the inverted tectonic stress field is reverse-type with roughly E–W compression. However, there were few available F-net data in the shallow crust (centroid depth $\leq$ 30 km) between January 1997

Table 2 List of focal mechanism solutions for large ($M_w \geq 6.0$) earthquakes with calculated rake angles and λ during Period II

No.	Year	Month	Day	Hour	Minute	Second	Longitude (deg.)	Latitude (deg.)	Depth (km)	M_w	Strike (deg.)	Dip angle (deg.)	Rake angle (deg.)	Region	Variance reduction (%)	Calculated rake angle (deg.)	Misfit angle (deg.)
30	2007	2	17	9	2	56.63	143.7227	41.7318	29	6.0	255	33	141	SE_OFF_ERIMOMISAKI	70.55	143.66	−2.66
31	2007	3	25	9	41	57.91	136.6860	37.2207	8	6.7	173	48	34	OFF_NOTO_PENINSULA	93.06	39.58	−5.58
32	2007	4	20	9	26	39.97	125.0710	25.7387	5	6.1	88	55	−62	NW_OFF_MIYAKOJIMA_ISLAND	86.84	−74.17	12.17
33	2007	4	20	10	45	54.93	125.1368	25.7478	5	6.1	117	48	−36	NW_OFF_MIYAKOJIMA_ISLAND	84.71	−40.96	4.96
34	2007	7	16	10	13	22.55	138.6095	37.5568	8	6.6	49	42	101	OFF_S_NIIGATA_PREF	90.54	93.22	7.78
35	2007	8	7	9	2	20.40	126.6680	27.3477	5	6.0	88	75	−46	NW_OFF_OKINAWAJIMA_IS	91.81	−47.77	1.77
36	2008	2	27	15	54	21.30	142.7383	26.8765	5	6.0	227	48	128	NEAR_CHICHIJIMA_ISLAND	90.28	149.58	−21.58
37	2008	3	15	7	32	7.39	143.1558	27.1048	5	6.2	3	32	120	NEAR_CHICHIJIMA_ISLAND	77.44	78.42	41.58
38	2008	5	8	1	2	0.30	141.9487	36.2312	26	6.2	16	64	87	FAR_E_OFF_IBARAKI_PREF	90.03	90.12	−3.12
39	2008	5	8	1	16	34.09	141.9788	36.2747	20	6.0	178	25	62	FAR_E_OFF_IBARAKI_PREF	82.42	66.23	−4.23
40	2008	6	14	8	43	45.36	140.8807	39.0298	5	6.9	209	51	104	SOUTHERN_IWATE_PREF	96.62	97.72	6.28
41	2008	9	11	9	20	51.35	144.1515	41.7755	29	6.8	269	36	159	SE_OFF_TOKACHI	75.96	134.61	24.39
42	2008	12	20	19	29	16.75	142.7000	36.5308	5	6.4	347	66	78	FAR_E_OFF_KANTO	87.66	58.30	19.70
43	2009	6	5	12	30	33.80	143.6203	41.8123	29	6.4	21	73	86	SE_OFF_ERIMOMISAKI	71.99	86.47	−0.47

Table 2 (continued)

No.	Year	Month	Day	Hour	Minute	Second	Longitude (deg.)	Latitude (deg.)	Depth (km)	M_w	Strike (deg.)	Dip angle (deg.)	Rake angle (deg.)	Region	Variance reduction (%)	Calculated rake angle (deg.)	Misfit angle (deg.)
44	2009	8	11	5	7	5.74	138.4993	34.7862	20	6.2	307	47	119	SOUTHERN_SURUGA_BAY_REG	86.01	136.77	−17.77
45	2010	5	26	17	53	7.19	129.9897	25.7423	8	6.4	201	52	−126	NEAR_MINAMI-DAITOJIMA_IS	75.81	−122.41	−3.59
46	2010	12	22	2	19	37.23	143.9350	27.052	5	7.3	107	59	−126	NEAR_CHICHIJIMA_ISLAND	70.84	−87.97	−38.03
47	2010	12	23	6	49	42.92	143.6887	26.9398	23	6.2	345	82	24	NEAR_CHICHIJIMA_ISLAND	85.02	24.19	−0.19
48	2011	3	9	11	45	12.97	143.2798	38.3285	23	7.2	186	23	70	FAR_E_OFF_MIYAGI_PREF	93.50	74.53	−4.53
49	2011	3	9	11	57	10.73	143.3973	38.3223	20	6.0	22	67	88	FAR_E_OFF_MIYAGI_PREF	68.64	87.90	0.10
50	2011	3	9	11	58	11.85	143.1552	38.2988	23	6.0	209	29	99	FAR_E_OFF_MIYAGI_PREF	59.24	95.96	3.04
51	2011	3	10	3	16	14.18	142.8788	38.2712	23	6.0	22	71	90	FAR_E_OFF_MIYAGI_PREF	86.64	81.48	8.52
52	2011	3	10	6	22	11.40	143.2187	38.1328	23	6.0	209	24	98	FAR_E_OFF_MIYAGI_PREF	84.64	97.22	0.78
53	2011	3	10	6	23	59.00	143.0448	38.1722	20	6.5	22	68	85	FAR_E_OFF_MIYAGI_PREF	80.78	80.62	4.38

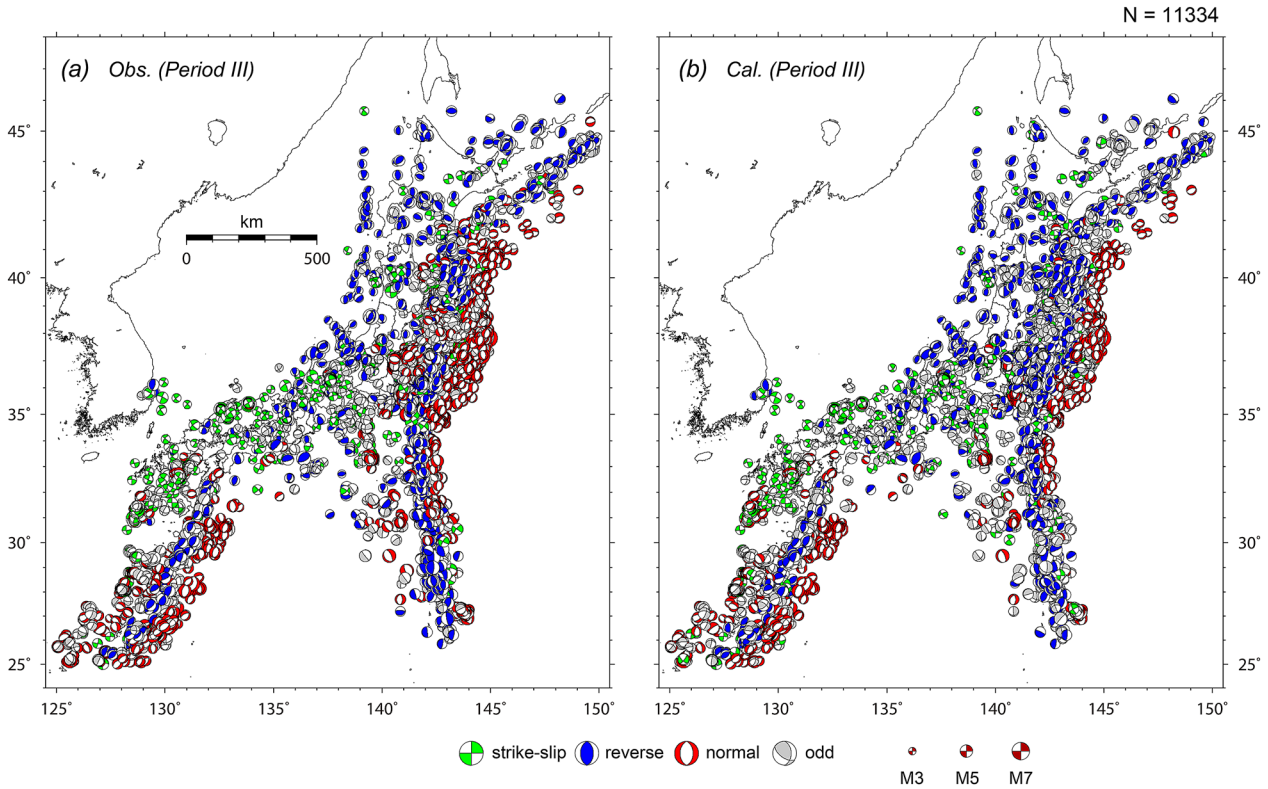

Fig. 11 **a** Distribution of F-net focal mechanism solutions of earthquakes that occurred in Period III. **b** Distribution of focal mechanism solutions with calculated rake angles from the 3D tectonic stress fields with WBH for Period III. The colors indicate fault types according to the classification criteria by Frohlich (1992)

and January 2007 in the region, and the uncertainty of inverted stress field was large.

Considering that the uncertainties of focal mechanism solutions generally range from 20 to 30° (e.g., Ishibe et al. 2014), our results support the applicability of the WBH method for evaluating the expected rake angles of future large earthquakes from recent tectonic stress fields. It is worth discussing the utilization of rake angles expected from tectonic stress fields with WBH for forecasting strong ground motions and tsunamis. In addition, our study also elucidates the necessity of close attention for applying this method for areas near the occurrences of large earthquakes, seismically inactive areas where the amount of available mechanism data to invert the stress is limited, and/or far offshore areas where the observation stations are sparsely distributed.

Possible causes of large $|\lambda|$

The resulting λ between the calculated rake angles and observed rake angles mostly ranged between $-30°$ and 30°, whereas they were large for the source region and nearby areas of major earthquakes such as the 2011 Tohoku-oki earthquake and regions with large uncertainties where the available focal mechanism data to invert the stress field of TM2010 are limited. Here, we discuss four possible causes of generating large $|\lambda|$.

Incomplete understanding of stress field

One possible explanation for the large $|\lambda|$ is an incomplete understanding of the stress field. The distribution of focal mechanism solutions from January 1997 to January 2007, which was used for the CMT data inversion, is spatially heterogeneous, and the uncertainties of the inverted stress field tend to be larger in the regions with a smaller number of available focal mechanism solutions. As mentioned, there were few available F-net data in the shallow crust (centroid depth $\leq$ 30 km) between January 1997 and January 2007 in the prefectural boundary region between Ibaraki and Fukushima (Figs. 14 and 15c). In the region, many earthquakes of normal faulting types with E–W tension suddenly increased immediately after the 2011 Tohoku-oki earthquake. Imanishi et al. (2012) found that microearthquakes of a normal faulting type occurred in the region before the 2011 Tohoku-oki earthquake and suggested that the stress field in the shallow crust was originally and locally a normal faulting regime, unlike other regions in the Tohoku district which are in E–W compression. This also suggests that

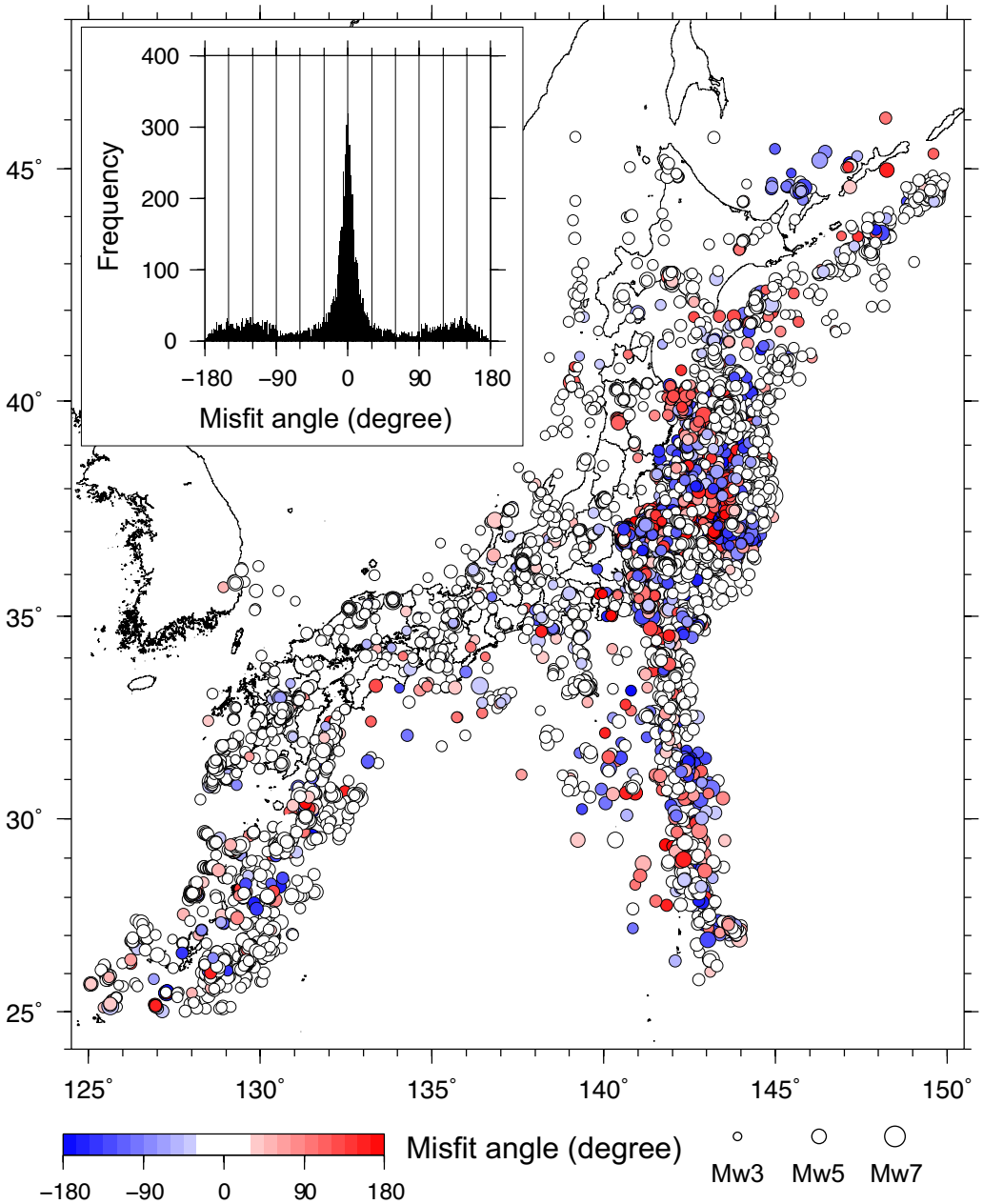

Fig. 12 Distribution of λ between the observed and calculated rake angles during Period III

coseismic stress changes by the 2011 Tohoku-oki earthquake revealed the local stress heterogeneity. The large $|\lambda|$ values in this region are attributed to large uncertainties of stress fields due to the lack of available focal mechanism solutions for the CMT data inversion by TM2010. The recent improvement of the CMT data inversion method to incorporate preceding inversion results into the update analysis as direct prior information about the stress field (Terakawa and Matsu'ura 2023) supports the results of Imanishi et al. (2012) and concludes that the proper stress field characterized by normal faulting appeared after the Tohoku-oki earthquake in the prefectural boundary region between Ibaraki and Fukushima. The M_w6.0 earthquake that occurred on 5th November 2018 near Kunashiri Island (No. 106 in Fig. 7c and Table 3) also occurred in a region where the available mechanism data are very limited (Fig. 15c).

A heterogeneity of the local tectonic stress regime and seismic activation in such regions also generates large $|\lambda|$. These regions have typically been highlighted by the

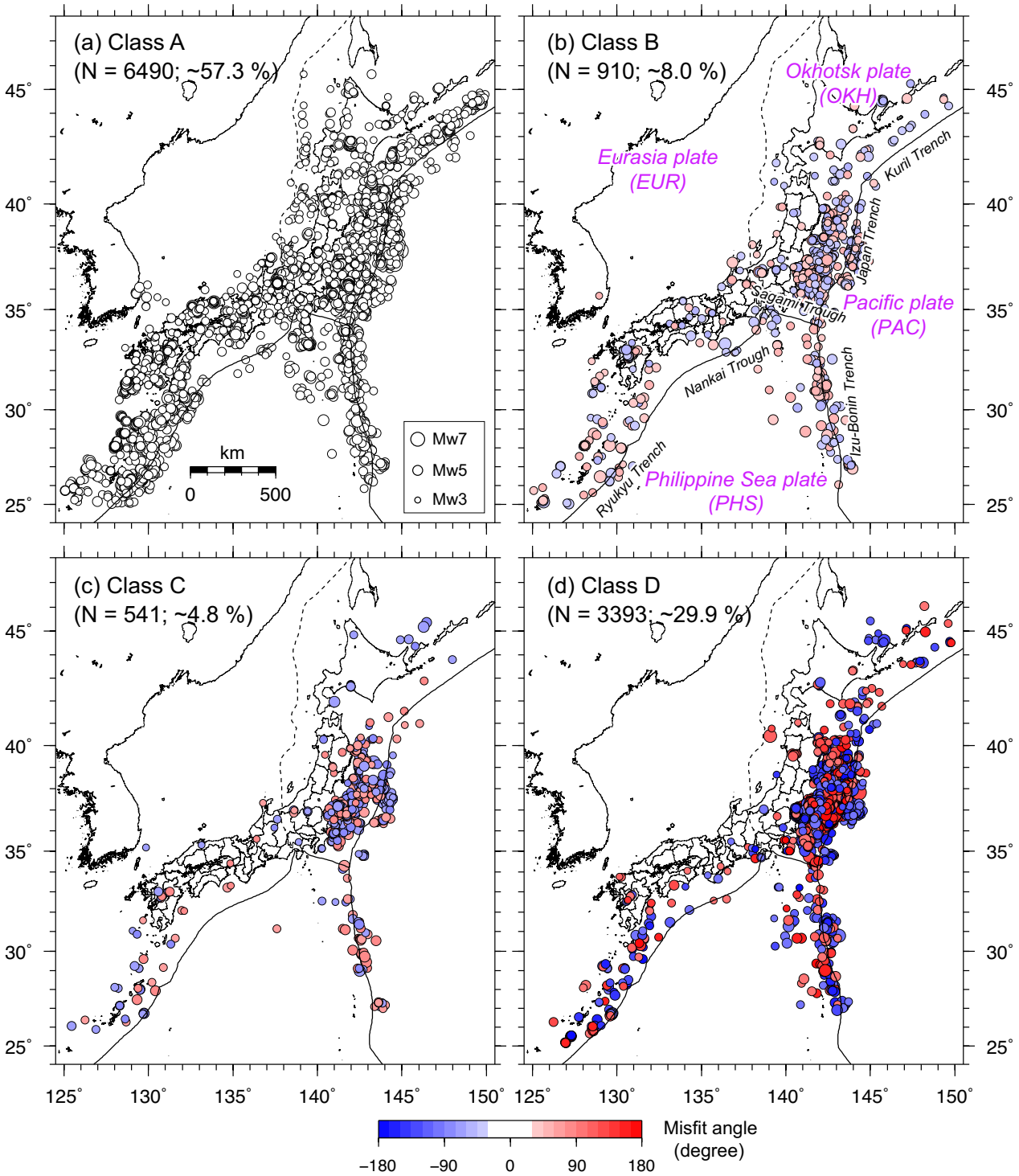

Fig. 13 Distribution of λ between the observed and calculated rake angles during Period III for **a** class A ($|\lambda| \leq 30°$), **b** class B ($30° < |\lambda| \leq 60°$), **c** class C ($60° < |\lambda| \leq 90°$) and **d** class D ($|\lambda| > 90°$)

stress increase imparted by major earthquakes (e.g., Toda et al. 2011; Terakawa et al. 2013; Terakawa and Matsu'ura 2023). In the Tohoku district, seismicity rates in most areas where the seismic activity drastically increased following the 2011 Tohoku-oki earthquake had been low for the preseismic period. The hypocenter distributions for both the periods are complementary each other (Fig. 16).

Table 3 List of focal mechanism solutions for large ($M_w \geq 6.0$) earthquakes with calculated rake angles and λ during Period III

No.	Year	Month	Day	Hour	Minute	Second	Longitude (deg.)	Latitude (deg.)	Depth (km)	M_w	Strike (deg.)	Dip angle (deg.)	Rake angle (deg.)	Region	Variance reduction (%)	Calculated rake angle (deg.)	Misfit angle (deg.)
54	2011	3	11	14	46	18.12	142.8610	38.1035	20	8.7	22	63	91	FAR_E_OFF_MIYAGI_PREF	71.75	98.01	−7.01
55	2011	3	11	15	25	44.40	144.8940	37.8367	20	7.6	12	41	−92	FAR_E_OFF_NORTH_HONSHU	83.58	−90.15	−1.85
56	2011	3	11	16	14	56.80	142.0688	36.5553	23	6.5	220	21	113	FAR_E_OFF_IBARAKI_PREF	66.51	119.89	−6.89
57	2011	3	12	0	13	12.15	142.0298	36.0373	11	6.1	87	33	158	FAR_E_OFF_IBARAKI_PREF	50.69	51.93	106.07
58	2011	3	12	3	59	15.62	138.5978	36.9860	5	6.2	242	38	117	MID_NII-GATA_PREF	74.52	113.18	3.82
59	2011	3	12	4	2	56.21	143.3052	39.2263	20	6.1	94	26	−64	FAR_E_OFF_SANRIKU	84.05	4.06	−68.06
60	2011	3	12	4	46	47.65	139.0697	40.4168	5	6.1	26	79	−152	W_OFF_AOMORI_PREF	84.79	96.56	111.44
61	2011	3	12	5	11	21.02	142.7725	38.8572	5	6.0	309	41	−93	FAR_E_OFF_MIYAGI_PREF	88.02	−114.31	21.31
62	2011	3	12	10	47	12.63	142.7565	37.4712	8	6.4	191	31	−127	FAR_E_OFF_FUKUSH-IMA_PREF	80.22	74.22	158.78
63	2011	3	13	10	26	2.08	141.9723	35.8282	8	6.2	123	66	−127	FAR_E_OFF_IBARAKI_PREF	83.07	−124.49	−2.51
64	2011	3	14	15	12	33.99	142.5877	37.8047	17	6.0	139	40	−177	SE_OFF_MIYAGI_PREF	73.22	44.72	138.28
65	2011	3	16	0	23	52.38	143.4743	40.3712	20	6.1	33	74	107	FAR_E_OFF_SANRIKU	78.22	107.58	−0.58
66	2011	3	22	16	18	40.84	144.2480	37.0860	8	6.3	209	42	−99	FAR_E_OFF_NORTH_HONSHU	77.26	−59.36	−39.64
67	2011	3	22	18	44	25.48	143.6610	39.9193	11	6.3	156	42	36	FAR_E_OFF_SANRIKU	80.86	36.55	−0.55

Table 3 (continued)

No.	Year	Month	Day	Hour	Minute	Second	Longitude (deg.)	Latitude (deg.)	Depth (km)	M_w	Strike (deg.)	Dip angle (deg.)	Rake angle (deg.)	Region	Variance reduction (%)	Calculated rake angle (deg.)	Misfit angle (deg.)
68	2011	3	22	18	46	13.68	141.2890	37.3328	26	6.1	331	55	−178	E_OFF_FUKUSHIMA_PREF	84.61	127.10	54.90
69	2011	3	28	7	23	57.02	142.3463	38.3837	20	6.1	281	67	−101	E_OFF_MIYAGI_PREF	84.19	−75.21	−25.79
70	2011	3	29	19	54	30.44	142.4697	37.4087	23	6.2	353	46	−130	SE_OFF_MIYAGI_PREF	74.58	86.08	143.92
71	2011	4	11	17	16	12.02	140.6727	36.9457	5	6.6	132	50	−82	EASTERN_FUKUSHIMA_PREF	86.83	34.30	−116.30
72	2011	4	12	8	8	15.89	140.8680	35.4817	26	6.3	304	77	162	NEAR_CHOSHI_CITY	68.62	154.57	7.43
73	2011	4	14	4	57	18.56	143.8072	39.6505	17	6.1	22	58	93	FAR_E_OFF_SANRIKU	81.42	89.80	3.20
74	2011	5	5	23	58	19.13	144.1190	38.2122	8	6.0	178	48	−122	FAR_E_OFF_NORTH_HONSHU	74.81	−98.60	−23.40
75	2011	8	17	20	44	8.67	143.7637	36.7687	5	6.1	46	35	−92	FAR_E_OFF_CENTRAL_HONSHU	77.94	67.07	−159.07
76	2011	9	17	4	26	35.86	143.0862	40.2592	20	6.7	26	77	100	NE_OFF_IWATE_PREF	88.08	98.48	1.52
77	2011	9	17	6	8	2.54	143.2128	40.2473	20	6.0	199	20	87	FAR_E_OFF_SANRIKU	75.74	78.98	8.02
78	2012	3	14	18	8	33.09	145.2275	40.7753	8	7.0	91	64	−87	FAR_SE_OFF_HOKKAIDO	89.44	−73.45	−13.55
79	2012	5	20	16	20	33.75	143.6212	39.5372	20	6.2	159	29	48	FAR_E_OFF_SANRIKU	69.57	45.65	2.35
80	2012	6	6	4	31	33.33	141.3707	34.9927	17	6.2	127	85	172	E_OFF_BOSO_PENINSULA	70.91	−55.76	−132.24
81	2012	10	2	7	21	42.63	143.5205	39.8328	20	6.0	40	74	110	FAR_E_OFF_SANRIKU	82.73	106.90	3.10
82	2012	12	7	17	18	20.28	144.3153	37.8158	11	7.3	6	77	−100	FAR_E_OFF_NORTH_HONSHU	80.85	135.62	124.38

Table 3 (continued)

No.	Year	Month	Day	Hour	Minute	Second	Longitude (deg.)	Latitude (deg.)	Depth (km)	M_w	Strike (deg.)	Dip angle (deg.)	Rake angle (deg.)	Region	Variance reduction (%)	Calculated rake angle (deg.)	Misfit angle (deg.)
83	2012	12	7	17	31	10.24	143.8557	37.9198	14	6.1	201	48	−93	FAR_E_OFF_MIYAGI_PREF	66.43	107.50	159.50
84	2013	4	2	3	53	15.74	143.5183	39.5053	20	6.0	27	72	96	FAR_E_OFF_SANRIKU	82.15	102.61	−6.61
85	2013	10	26	2	10	18.39	144.5687	37.1963	20	7.1	12	46	−80	FAR_E_OFF_NORTH_HONSHU	94.80	−70.07	−9.93
86	2014	7	12	4	22	0.44	142.3208	37.0500	5	6.5	346	63	−123	E_OFF_FUKUSH-IMA_PREF	75.91	106.23	130.77
87	2014	11	22	22	8	17.90	137.8910	36.6928	5	6.3	25	50	65	NORTHERN_NAGANO_PREF	73.78	86.31	−21.31
88	2015	2	17	8	6	34.68	143.1927	39.8723	17	6.7	24	70	98	FAR_E_OFF_SANRIKU	91.15	98.34	−0.34
89	2015	2	20	13	25	20.99	143.7322	39.9127	11	6.1	28	61	108	FAR_E_OFF_SANRIKU	90.27	100.37	7.63
90	2015	2	25	16	0	59.32	142.1370	31.0890	5	6.1	338	77	87	NEAR_TOR-ISHIMA_IS	74.56	53.31	33.69
91	2015	5	11	6	25	44.84	142.1460	31.2318	5	6.1	338	69	87	NEAR_TOR-ISHIMA_IS	65.96	72.16	14.84
92	2015	5	31	3	49	6.29	143.1283	30.7745	5	6.1	137	35	−105	FAR_E_OFF_IZU_ISLANDS	68.33	−12.98	−92.02
93	2015	9	2	0	25	10.23	142.1410	31.4665	5	6.0	337	75	85	NEAR_TOR-ISHIMA_IS	65.12	95.70	−10.70
94	2015	11	14	5	51	30.11	128.5900	30.9432	17	6.8	96	71	−10	SW_OFF_KYUSHU	92.03	−12.82	2.82
95	2016	4	14	21	26	34.43	130.8087	32.7417	17	6.1	212	89	−164	NW_KUMA-MOTO_PREF	91.24	166.35	29.65
96	2016	4	15	0	3	46.45	130.7777	32.7007	8	6.0	119	62	−4	NW_KUMA-MOTO_PREF	93.90	0.91	−4.91
97	2016	4	16	1	25	5.47	130.7630	32.7545	11	7.1	131	53	−7	NW_KUMA-MOTO_PREF	94.08	−6.80	−0.20
98	2016	8	20	18	1	23.64	143.7788	40.3668	11	6.0	153	38	33	FAR_E_OFF_SANRIKU	75.13	30.05	2.95

Table 3 (continued)

No.	Year	Month	Day	Hour	Minute	Second	Longitude (deg.)	Latitude (deg.)	Depth (km)	M_w	Strike (deg.)	Dip angle (deg.)	Rake angle (deg.)	Region	Variance reduction (%)	Calculated rake angle (deg.)	Misfit angle (deg.)
99	2016	9	21	1	21	15.71	142.3207	30.5518	5	6.0	180	25	111	NEAR_TORISHIMA_IS	78.54	15.96	95.04
100	2016	9	23	9	14	31.35	141.8438	34.3963	11	6.2	352	54	94	FAR_SE_OFF_BOSO_PEN	91.89	68.34	25.66
101	2016	10	21	14	7	22.57	133.8562	35.3805	8	6.2	342	80	9	EASTERN_TOTTORI_PREF	93.13	15.96	−6.96
102	2016	11	22	5	59	46.89	141.6042	37.3547	11	7.0	227	52	−90	E_OFF_FUKUSHIMA_PREF	96.48	124.93	145.07
103	2017	9	21	1	37	18.59	144.4887	38.0360	20	6.2	34	27	−76	FAR_E_OFF_NORTH_HONSHU	95.64	−77.19	1.19
104	2017	10	6	16	59	32.89	143.9483	37.4353	8	6.1	51	48	−53	FAR_E_OFF_NORTH_HONSHU	80.78	−37.26	−15.74
105	2017	11	9	16	42	10.88	141.4687	32.6405	5	6.0	349	70	86	E_OFF_HACHIJOJIMA_ISLAND	86.47	70.39	15.61
106	2018	11	5	4	26	1.67	145.8065	44.6083	5	6.0	1	31	57	NEAR_KUNASHIRI_ISLAND	86.92	−176.90	−126.10
107	2019	1	8	21	39	30.08	131.1645	30.5725	23	6.3	52	58	103	NEAR_TANEGASHIMA_ISLAND	90.79	132.89	−29.89
108	2019	4	11	17	18	18.14	143.4048	40.3625	20	6.0	185	23	68	FAR_E_OFF_SANRIKU	88.31	68.55	−0.55
109	2019	5	10	8	48	41.68	131.9745	31.8012	26	6.2	208	33	84	HYUGANADA_REGION	92.45	88.59	−4.59
110	2019	6	18	22	22	19.98	139.4793	38.6080	11	6.4	23	36	86	W_OFF_YAMAGATA_PREF	89.36	85.00	1.00
111	2019	12	11	2	5	2.23	141.9698	30.7758	5	6.0	355	79	94	NEAR_TORISHIMA_IS	76.80	56.57	37.43
112	2020	5	3	20	54	21.08	128.7168	31.3037	5	6.0	170	77	−160	SW_OFF_KYUSHU	91.07	−173.20	13.20

Table 3 (continued)

No.	Year	Month	Day	Hour	Minute	Second	Longitude (deg.)	Latitude (deg.)	Depth (km)	M_w	Strike (deg.)	Dip angle (deg.)	Rake angle (deg.)	Region	Variance reduction (%)	Calculated rake angle (deg.)	Misfit angle (deg.)
113	2021	11	29	21	40	47.07	142.3770	31.2927	5	6.2	157	38	−102	NEAR_TORISHIMA_IS	67.02	31.84	−133.84
114	2021	12	9	11	5	8.01	129.4505	29.3428	5	6.0	92	31	−30	NEAR_TOKARA_ISLANDS	87.19	−32.03	2.03

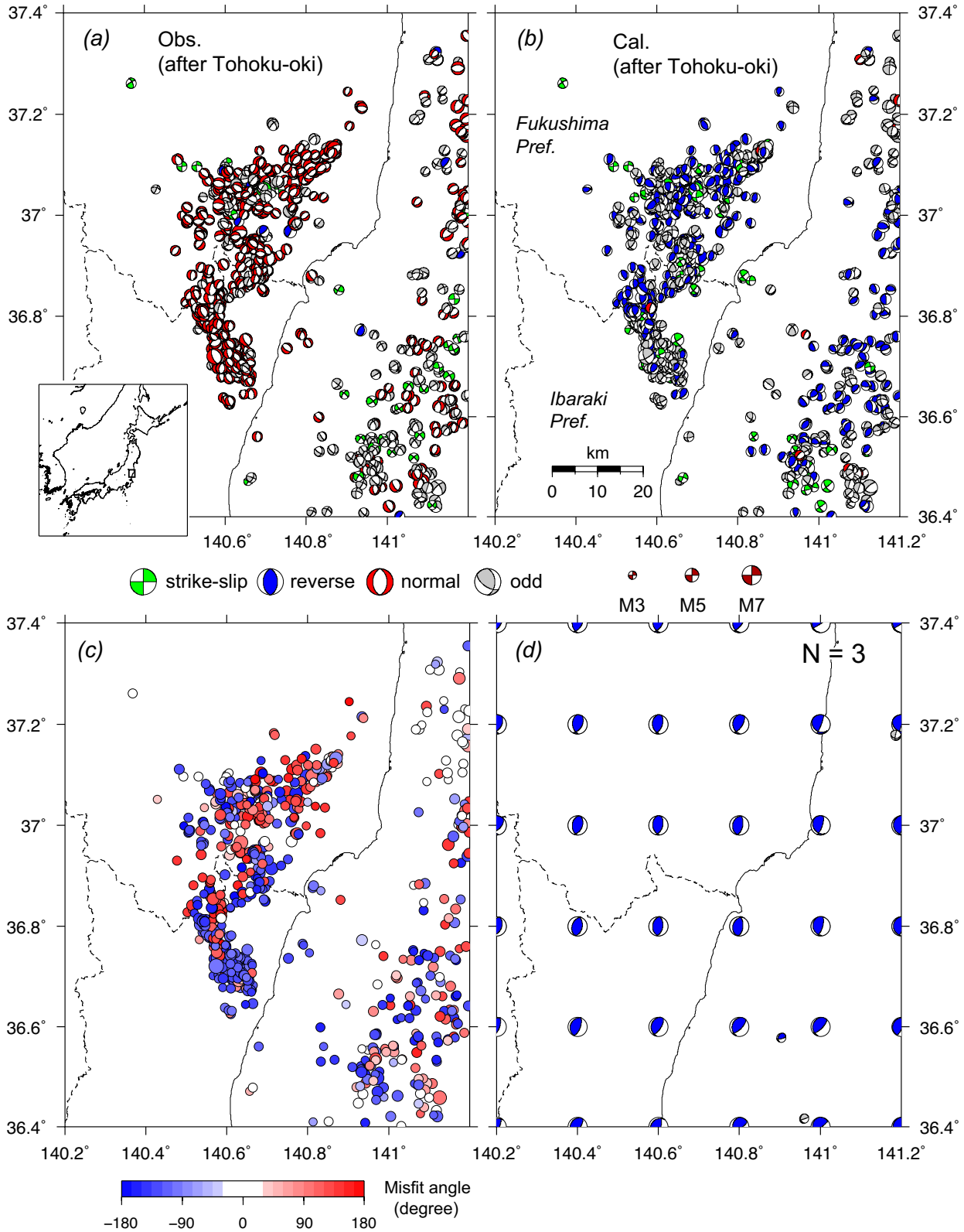

Fig. 14 Distribution of focal mechanism solutions for earthquakes with **a** observed and **b** calculated rake angles in the prefectural boundary region between Fukushima and Ibaraki during Period III. **c** Distribution of λ between the observed and calculated rake angles during Period III. **d** Regional tectonic stress field by Terakawa and Matsu'ura (2010) at a depth of 10 km and distribution of F-net mechanism solutions for earthquakes with centroid depths ≤ 30 km spanning from January 1997 to January 2007 that were used for the CMT data inversion

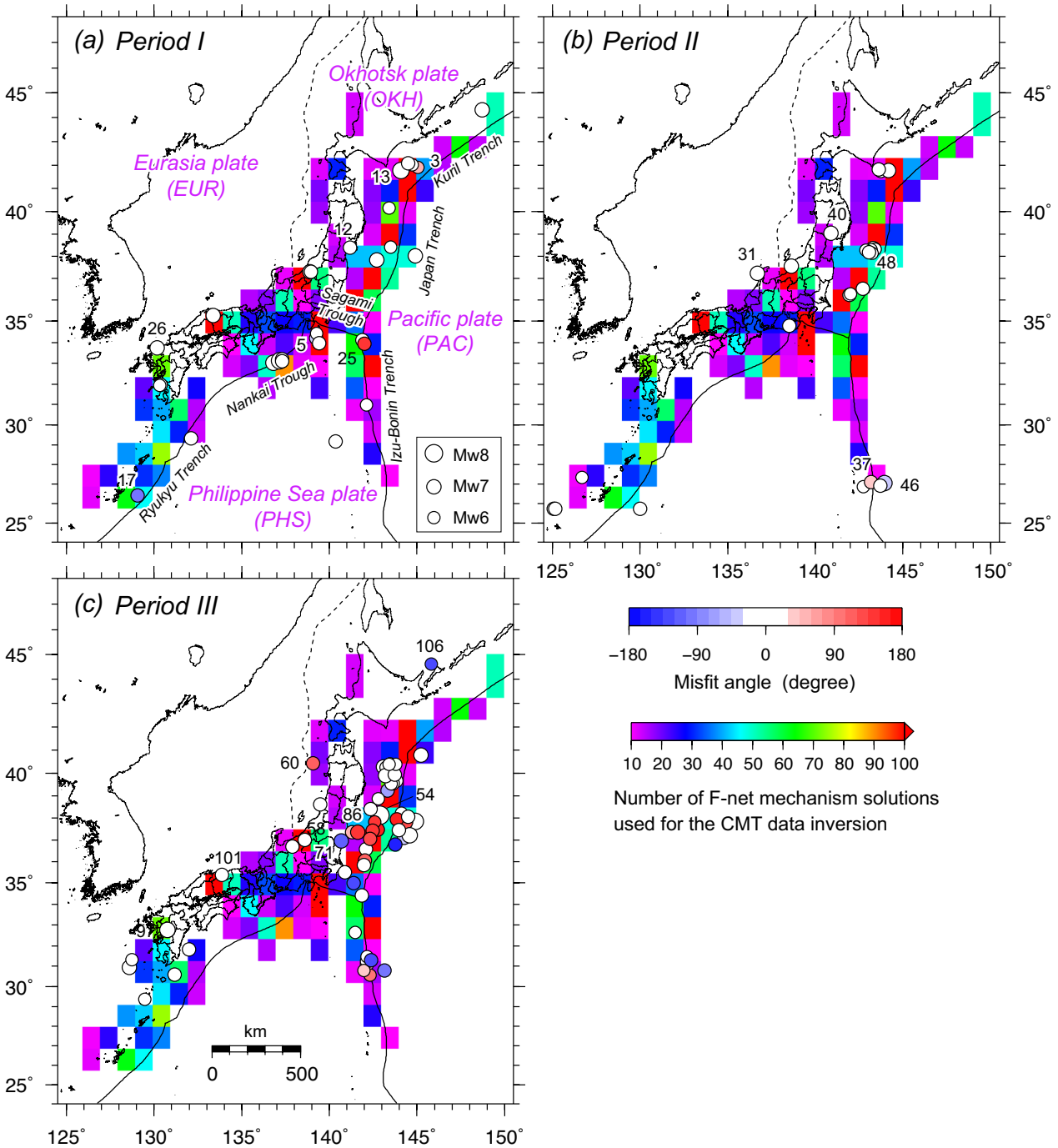

Fig. 15 Distribution of λ for large ($M_w \geq 6.0$) earthquakes that occurred during **a** Period I, **b** Period II, and **c** Period III with the number of F-net mechanism solutions used for CMT data inversion (from January 1997 to January 2007) at a spacing of 1.0° × 1.0° for ≥ 10 mechanism data points. The numbers in the figures are the IDs in Tables 1, 2, 3

Coseismic stress change

Another possible explanation for large $|\lambda|$ is coseismic stress changes, especially in the source and nearby regions of major earthquakes. Occurrences of earthquakes perturb the stress field and cause changes in seismicity (e.g., Stein et al. 1992; King et al. 1994; Toda et al. 1998; Ishibe et al. 2011b). Temporal changes in λ (Fig. 17) showed that earthquakes with large $|\lambda|$ explosively increased after the occurrences of major earthquakes (e.g., the 2011 Tohoku-oki earthquake) and then

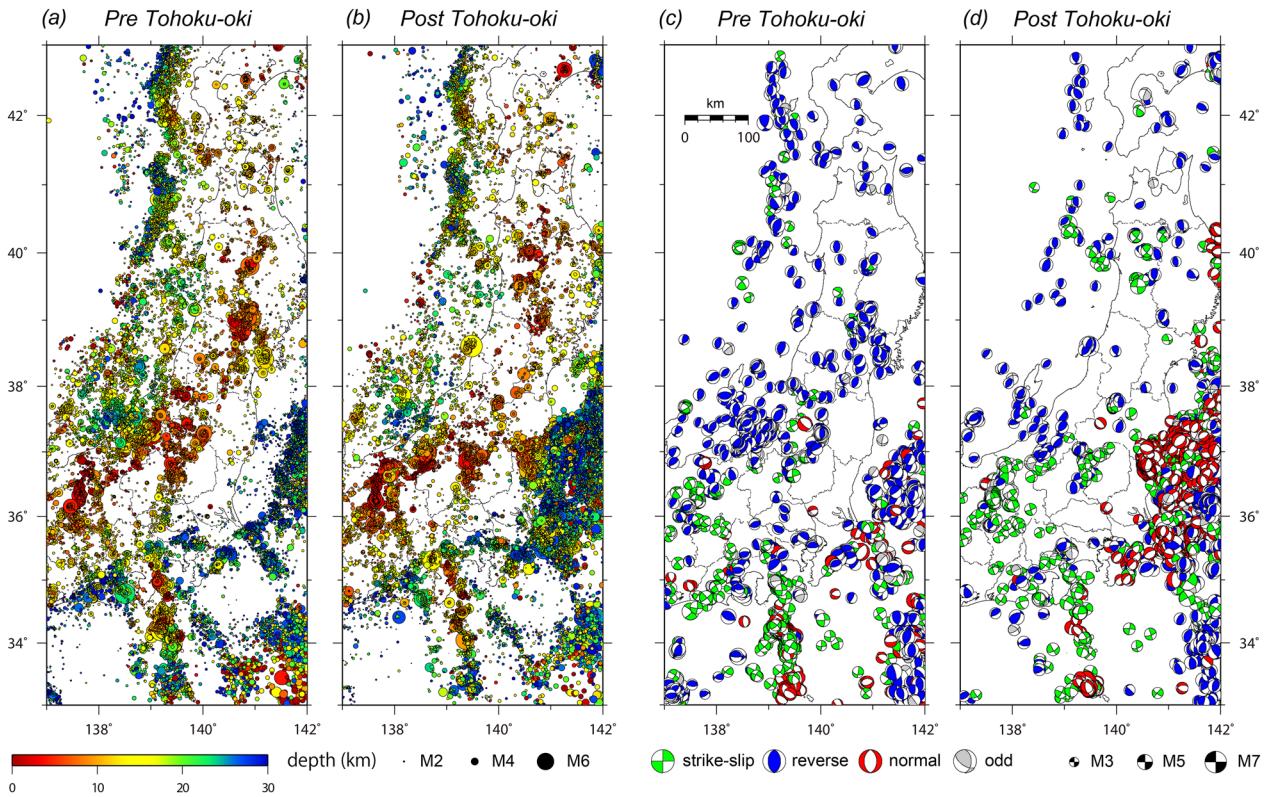

Fig. 16 **a** Hypocenter distribution of earthquakes during **a** preseismic (October 1997—occurrence time of the 2011 Tohoku-oki earthquake) and **b** postseismic (2011 Tohoku-oki earthquake—December 2020) periods. The colors indicate the hypocentral depths. **c** Distribution of F-net mechanisms and their fault types according to the criteria by Frohlich (1992) for **c** preseismic and **d** postseismic periods

gradually decayed with time. The $|\lambda|$ values can be large even for regions where seismicity was originally high and the stress field was reliably inverted by abundant focal mechanism data in and near the source region of the 2011 Tohoku-oki earthquake (Figs. 12 and 13). For example, the M_w6.5 earthquake (No. 86 in Fig. 7c and Table 3) that occurred on 12th July 2014 east off Fukushima Prefecture exhibits a large $|\lambda|$ ($\lambda = 130.77°$), while the number of focal mechanism data to invert the stress field is relatively large (Fig. 15c). Terakawa and Matsu'ura (2023) pointed out that the stress orientation change in a region off Fukushima and Ibaraki, the southern margin of the main rupture area of the megathrust event, seems to be real. The concentration of focal mechanism solutions with large $|\lambda|$ during Period III coincides well with the above region. However, coseismic stress changes in inland regions and coastal regions of the Sea of Japan of the Tohoku district are too small to alter the stress orientation (Terakawa et al. 2013).

The $|\lambda|$ values can also be larger due to transient stress changes, for example, accompanied by slow slip events. The $|\lambda|$ value exceeds 30° for the M_w6.0 earthquake which occurred on 9th October 1997 (No. 3 in Fig. 7a and Table 1), approximately 6 years before the 2003 Tokachi-oki earthquake (No. 13 in Fig. 7a and Table 1). Based on an analysis of GPS data and seismicity, it was suggested that the deeper half of the plate interface within the rupture area of the 2003 Tokachi-oki earthquake was uncoupled and that a slow slip event occurred in several years prior to the mainshock (e.g., Baba and Hori 2006; Ogata 2005). The large $|\lambda|$ value might be related to transient stress changes imparted by a slow slip event (e.g., Katsumata 2011).

Local deviatoric stress changes caused by the pore-fluid pressure increase

Another possible explanation for the large $|\lambda|$ is the local deviatoric stress changes caused by the pore-fluid pressure increase, enforced by the intrusion of high-pressure fluid into a fault zone (Matsu'ura and Terakawa 2021). One representative example is the concentration of large $|\lambda|$ in the source region of the 2011 Tohoku-oki earthquake (Fig. 7c). These events have focal mechanisms of normal faulting with E–W tension, which are largely deviated from the stress pattern in TM2010. Terakawa and Matsu'ura (2023) concluded that strong shaking by

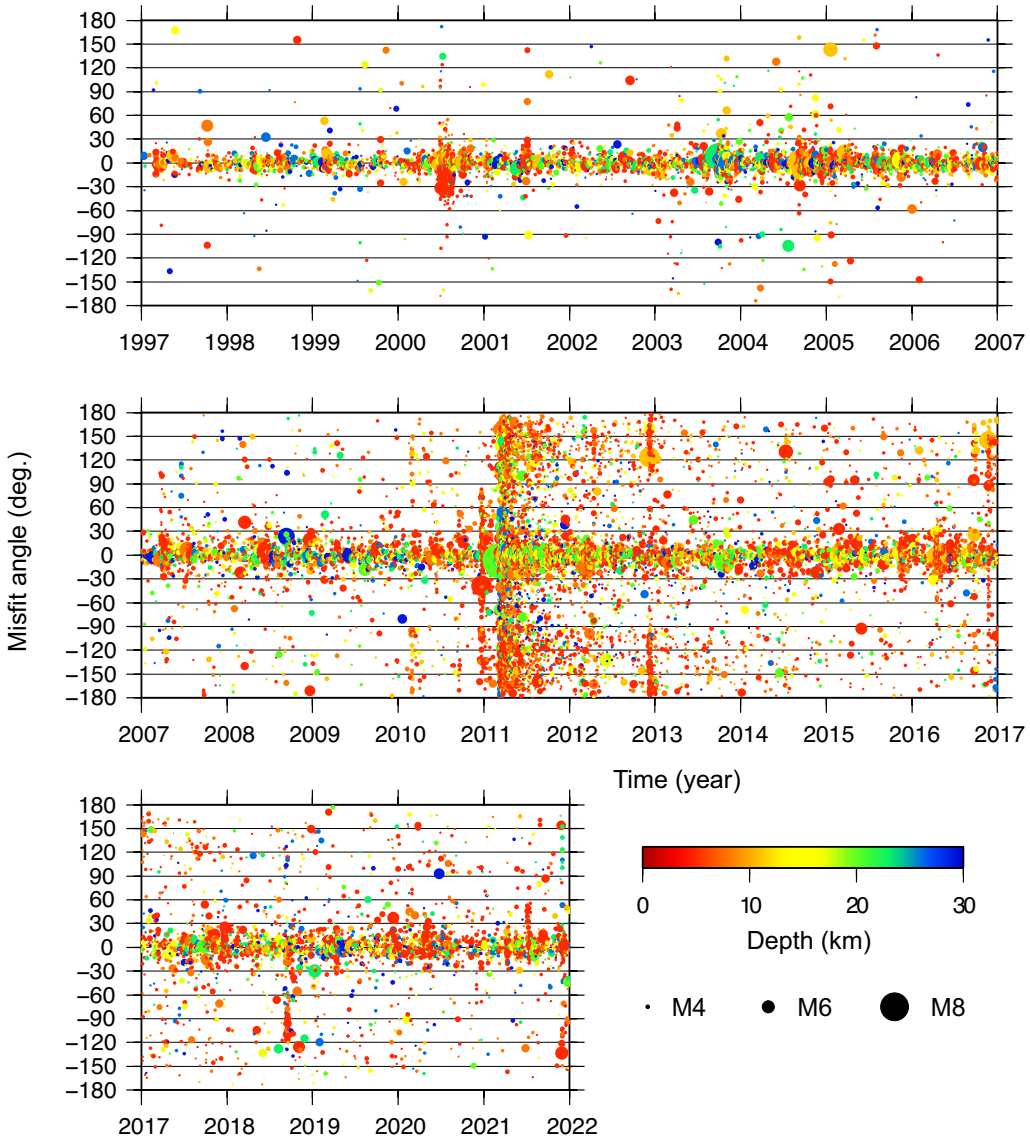

Fig. 17 Occurrence times of earthquakes vs. λ

the 2011 Tohoku-oki earthquake resulted in a wide damage zone around the main rupture fault and that the rapid intrusion of high-pressure fluid through the suddenly developed fluid-path network triggered clustered events with abnormal focal mechanisms at shallower depths. Matsu'ura and Terakawa (2021) mathematically indicated that the fault orientations of aftershocks are not necessarily consistent with the surrounding deviatoric stress field when the enforced pore-fluid pressure changes, driven by the intrusion of high-pressure fluid into an accidentally chosen preexisting fault from deep reservoirs, are dominant. However, the activity of these events rapidly decreased within a year (Terakawa and Matsu'ura 2023), indicating that they are not the indicators of tectonic stress fields. Therefore, large $|\lambda|$ values which come from these events do not undermine the applicability of the method estimating realistic rake angles for reliable prediction of strong ground motions and tsunamis caused by future large earthquakes.

Uncertainties of moment tensor solutions

Uncertainties of moment tensor solutions can also be a factor generating large $|\lambda|$, and they are basically larger for offshore regions than for inland regions due to the sparse distribution of seismograph observation stations. Variance reductions (VR), which indicate the fit between

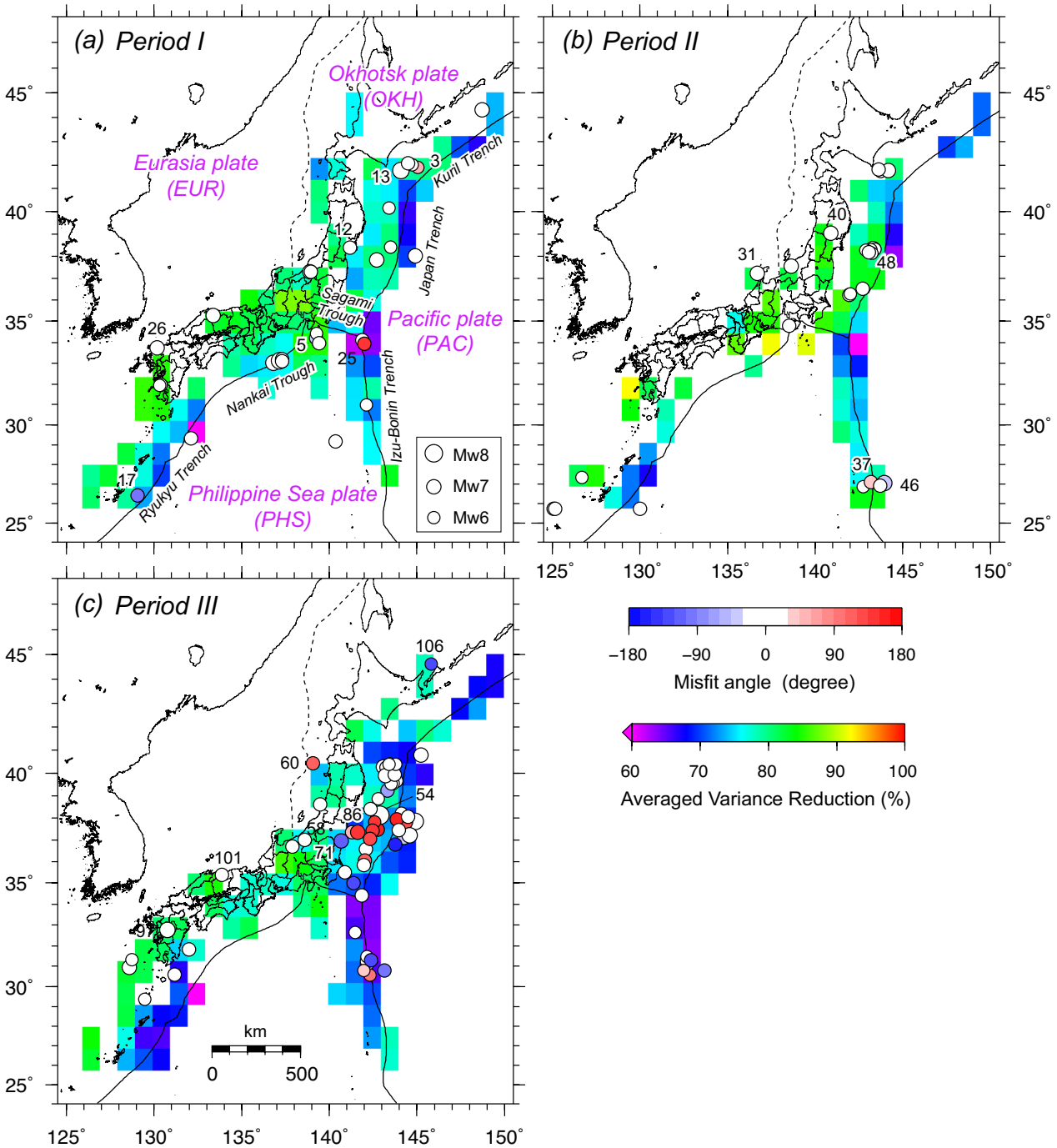

Fig. 18 Comparison of λ for large ($M_w \geq 6.0$) earthquakes with the distribution of averaged variance reductions (VR) for 1.0° × 1.0° spacing in longitudes and latitudes where the number of available mechanism data is ≥ 10 during **a** Period I, **b** Period II, and **c** Period III

observed and synthetic waveforms, are comparatively low for the focal mechanism solutions of earthquakes that occurred in the offshore region (Fig. 18 and Additional file 26: Fig. S26, e.g., along the Izu–Bonin and Ryukyu Trenches). Relatively large $|\lambda|$ values in these regions (e.g., the M_w6.5 earthquake that occurred on 19th January 2005 in the far southeastern off Boso Peninsula near the triple junction among the Pacific, Philippine, and Okhotsk plates (No. 25 in Fig. 7a and Table 1)) are possibly due to the large uncertainties of centroid

location and/or moment tensor solutions. For the M_w6.2 earthquake that occurred on 15th March 2008 near Chichi-jima Island along the Izu–Bonin Trench (Period II), which showed a large $|\lambda|$ (41.58°; No. 37 in Fig. 7b and Table 2), the centroid depth of 5 km is significantly shallower than the hypocentral depth (66 km) determined by the JMA. Relatively large misfit angles are possibly due to both the large estimation errors of the stress field due to the relatively low quality of mechanism solutions and the large uncertainties of CMT solutions themselves that were used for validation. Recently, a large-scale seafloor observation network for earthquakes and tsunamis consisting of 150 observatories (S-net) was established in the Japan Trench area by NIED (Aoi et al. 2020). Furthermore, another seafloor observation network called N-net is now under construction in the Nankai Trough subduction zone by NIED. These networks will contribute to a better understanding of the stress field, reduce $|\lambda|$ and uncertainties in the hypocentral location and improve early tsunami warning capabilities.

Application to fault zones in the Kyushu District

In the Kyushu district, southwest Japan, 16 FZs are evaluated as major Quaternary active FZs by the HERP. In addition, 17 faults are evaluated as short faults in the Regional Evaluation of Active Faults in the Kyushu District (1st edition) (HERP 2013). We analyze 16 FZs and two short faults whose fault models are developed by J-SHIS. In the northern part of the Kyushu district, left-lateral faults striking roughly NW–SE directions predominate, and they are distributed at intervals of approximately 10–20 km (Fig. 19a). Conjugated right-lateral faults striking roughly NE–SW directions are also distributed in some parts of the district. In the central and southern parts, right-lateral faults and normal faults reflecting their N–S extension field are mixed.

The fault types inferred from the 3D tectonic stress field by TM2010 with WBH generally reproduce the above regional characteristics well, with left-lateral fault types predominating in the northern part and right-lateral and normal fault types predominating in the central and southern parts (Fig. 19 and Table 4). Among 32 fault segments (FSs), fault types predicted by the method coincide with the HERP evaluation for 25 FSs (~ 78.1%). For example, left-lateral faults distributed in the northern part of the Kyushu district (i.e., Nishiyama FZ, Umi F, Hinata-toge-Okasagi-toge FZ and Kego FZ) are well reproduced by the method. The Izumi F is classified as a right-lateral fault by the method in the present study, while the HERP evaluated as a normal fault, including a right-lateral component. However, the calculated rake angle is − 135.65° and is near the classification boundary between the right-lateral and normal faults. The northeastern and southeastern parts of the Koshiki FZ (Koshiki segment) have been evaluated as a north-uplifting normal fault with left-lateral displacement and a northwest-uplifting normal fault, respectively (HERP 2013), while they are estimated to be mainly strike-slip faults from the method. The Ichiki segment, Koshiki-Kaikyo central segment, and Fukiagehama seiho-oki segment of the Ichiki FZ are evaluated as "normal fault with right-lateral component", "normal fault whose strike-slip component is unknown", and "normal fault whose strike-slip component is unknown", respectively (HERP 2013). The fault types inferred from the method in the present study are mainly strike-slip faults.

The 2016 Kumamoto earthquake sequence ruptured the Takano-Shirahata segment of the Hinagu FZ and the Futagawa segment of the Futagawa FZ. The largest foreshock occurred on 14th April 2016 (M_w6.1), with an F-net rake angle of − 164°, and this event was evaluated as the rupture of the northern segment (Takano-Shirahata segment) of the Hinagu FZ, a right-lateral fault striking NE–SW. The mainshock on 16th April 2016 (M_w7.1) ruptured the Futagawa FZ with an F-net rake angle of − 142°. λ is 29.65° for the largest foreshock and − 0.20° for the mainshock. The geomorphologically and geologically evaluated fault types and the observed and calculated rake angles are consistent with each other for both FZs. The fault types for the Futagawa segment of the Futagawa FZ and Takano-Shirahata segment for the Hinagu FZ are evaluated as right-lateral faults. The rake angles calculated from the 3D tectonic stress field with WBH were − 168.267° for the Futagawa segment of the Futagawa FZ and 179.84° for the Takano-Shirahata segment of the Hinagu FZ, and they were also classified as right-lateral faults. These results are consistent with a previous study (Matsumoto et al. 2018) that indicated that the prestate of stress on the fault controls the slip direction of complicated coseismic fault slip for the 2016 Kumamoto earthquake.

The calculated rake angles depend on both the regional stress field and fault geometry, and the robustness of converted fault types may differ from each fault. Furthermore, mismatch between the fault types estimated from the method and geomorphologically and geologically evaluated fault types may be due to uncertainties in the geometry of the targeted faults. In particular, the dip angles are sometimes poorly constrained and are conventionally set to some representative values for forecasting strong ground motions and tsunamis. The comparison (mismatch) of fault types obtained from geomorphology and geology with those from the method in this study would provide a valuable opportunity for the reexamination of fault types and fault geometries.

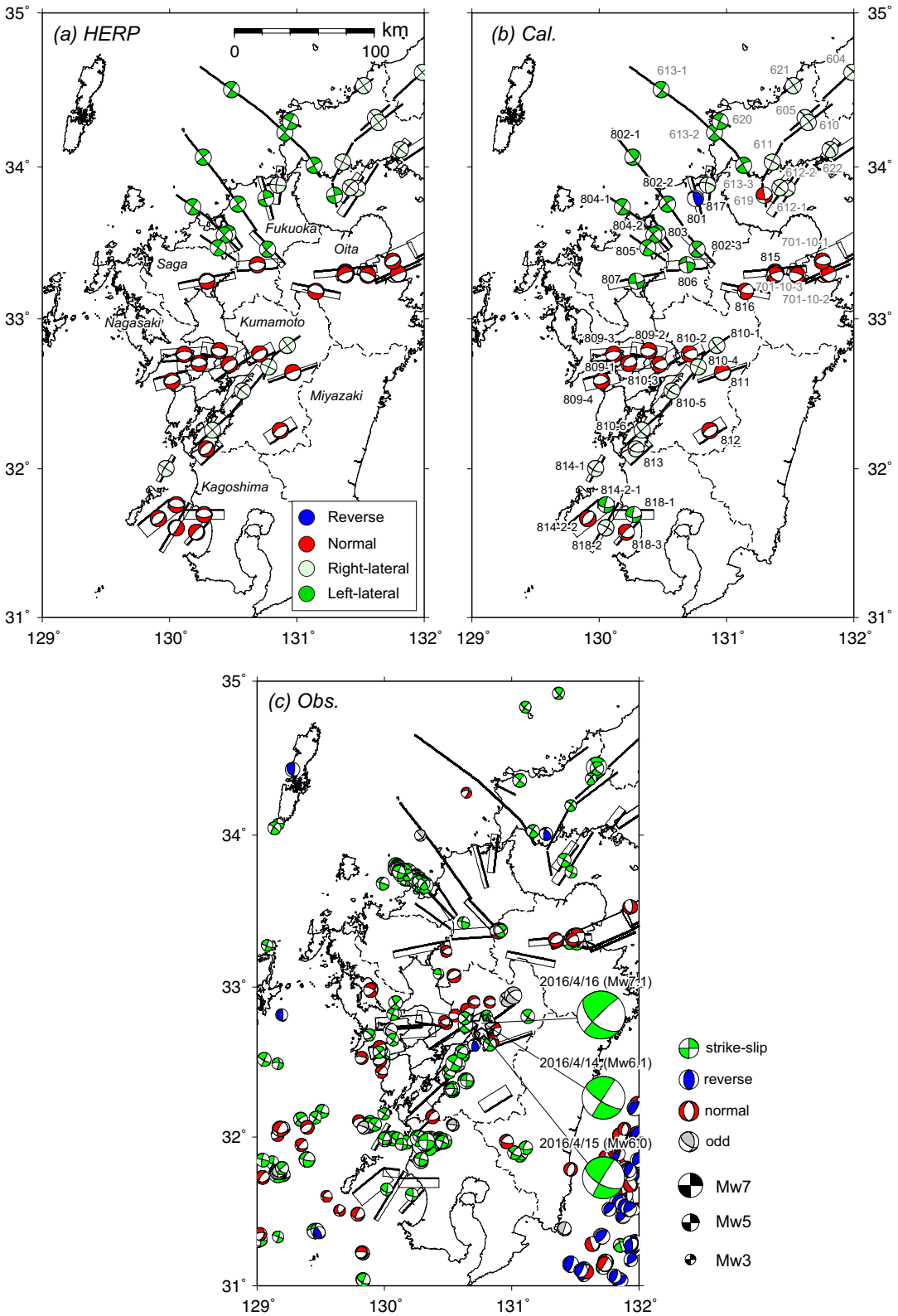

Fig. 19 **a** Types of faulting for the Quaternary major active faults that were evaluated by the Headquarters for Earthquake Research Promotion (HERP). **b** Calculated rake angles for the Quaternary major active faults that were evaluated by HERP. A type of faulting for each fault is converted from the calculated rake angle (see the text for the classification criteria). **c** F-net mechanism solutions for earthquakes that occurred from January 1997 to December 2021. The colors indicate fault types according to the classification criteria by Frohlich (1992)

Table 4 Quaternary active faults in Kyushu district, southwest Japan, that were evaluated by HERP and the fault models were developed by J-SHIS from NIED, and the geomorphologically and geologically evaluated fault types were compared with those inferred from the regional stress field with WBH

Fault ID	Segment ID	Fault zone (FZ) name	Segment name	Longitude (degree)	Latitude (degree)	Top depth (km)	Fault length (km)	Fault width (km)	Fault strike (degree)	Dip angle (degree)	Direction of dip	Fault type by HERP[a]	Calculated rake angle (degree)	Fault type[a]	Type match	Slip rate strike-slip component (mm/yr)	Slip rate vertical component (mm/yr)	Average recurrence interval (yrs)
801	801	Fukuchiyama FZ		130.726	33.936	3	32	12	165	75	W	LL (+R)	107.01	R	N	–	0.02–0.03	9400–32000
802	802-1	Nishiyama FZ	Oshima-oki segment	130.122	34.212	2	42	16	142	90	–	LL	40.83	LL	Y	–	–	–
802	802-2	Nishiyama FZ	Nishiyama segment	130.387	33.932	2	48	16	144.8	90	–	LL	−12.28	LL	Y	–	–	–
802	802-3	Nishiyama FZ	Kamatoge segment	130.658	33.583	2	34	16	136.5	75	–	LL	−9.55	LL	Y	–	–	–
803	803	Umi F		130.405	33.684	2	28	14	146.7	62.5	W	LL (+R)	−2.10	LL	Y	–	0.02–0.03	20,000–30000
804	804-1	Kego FZ	Northwestern segment	130.313	33.659	2	30	16	306	90	–	LL	−7.36	LL	Y	–	–	–
804	804-2	Kego FZ	Southeastern segment	130.309	33.656	2	32	16	136	90	SW	LL	−12.52	LL	Y	–	0.02	3100–5500
805	805	Hinata-toge-Okasagi-toge FZ		130.521	33.384	2	32	14	305.5	90	–	LL	19.02	LL	Y	–	–	–
806	806	Minou FZ		130.853	33.334	3	30	14	266	60	N	N	0.84	LL	N	–	0.2	14,000
807	807	Sagaheiya-hokuen FZ		130.067	33.233	3	42	14	78.7	70	S	N	−5.01	LL	N	–	0.2–0.5	6600–19000
809	809-1	Unzen FG	Northern part	130.057	32.734	3	32	18	86.2	60	S	N	−58.67	N	Y	–	–	–
809	809-2	Unzen FG	Southeastern part	130.519	32.730	3	26	18	279	60	N	N	−75.89	N	Y	–	–	–
809	809-3	Unzen FG	Southwestern part (Northern segment)	130.298	32.733	3	34	18	266.6	60	N	N	−73.16	N	Y	–	1.0	2500–4700

Table 4 (continued)

Fault ID	Segment ID	Fault zone (FZ) name	Segment name	Longitude (degree)	Latitude (degree)	Top depth (km)	Fault length (km)	Fault width (km)	Fault strike (degree)	Dip angle (degree)	Direction of dip	Fault type by HERP[a]	Calculated rake angle (degree)	Fault type[a]	Type match	Slip rate strike-slip component (mm/yr)	Slip rate vertical component (mm/yr)	Average recurrence interval (yrs)
809	809-4	Unzen FG	South-western part (Southern segment)	129.872	32.598	3	26	18	75.8	60	S	N	−105.35	N	Y	–	≥0.3	2100–6500
810	810-1	Futagawa FZ	Futagawa segment	131.027	32.888	3	24	14	233.2	90	NW	RL	−168.27	RL	Y	0.2	0.1–0.3	8100–26000
810	810-2	Futagawa FZ	Uto segment	130.831	32.780	3	22	16	243.2	60	NW	N	−127.88	N	Y	–	(≥) 0.2–0.5	–
810	810-3	Futagawa FZ	Uto-hanto-hokugan segment	130.637	32.748	3	32	16	236.1	60	NW	N	−129.25	N	Y	–	–	–
810	810-4	Hinagu FZ	Takano-Shirahata segment	130.819	32.763	3	20	14	202.9	90	–	RL	179.84	RL	Y	–	0.04–0.2	–
810	810-5	Hinagu FZ	Hinagu segment	130.751	32.653	3	44	16	218.6	60	NW	RL	−166.19	RL	Y	0.7	0.2–0.5	3600–11000
810	810-6	Hinagu FZ	Yatsu-shirokai segment	130.469	32.363	3	34	14	227.3	90	–	RL	−163.52	RL	Y	–	–	1100–6400
811	811	Midori-kawa FZ		131.163	32.691	2	38	12	250.8	80	N	N (+RL)	−91.13	N	Y	–	0.05–0.1	34,000–68000
812	812	Hitoyoshi-bonchi-nanen F		131.003	32.280	2	24	18	238	60	NW	N	−94.23	N	Y	–	0.1–0.2	≥8000
813	813	Izumi FZ		130.420	32.159	3	22	18	227.6	45	NW	N (+RL)	−135.65	RL	N	–	0.1–0.2	8000
814	814-1	Koshiki FZ	Northeastern-off-Kamikoshiki-jima segment	130.045	32.080	2	22	12	211.3	75	–	RL	−157.22	RL	Y	–	–	–

Table 4 (continued)

Fault ID	Segment ID	Fault zone (FZ) name	Segment name	Longitude (degree)	Latitude (degree)	Top depth (km)	Fault length (km)	Fault width (km)	Fault strike (degree)	Dip angle (degree)	Direction of dip	Fault type by HERP[a]	Calculated rake angle (degree)	Fault type[a]	Type match	Slip rate strike-slip component (mm/yr)	Slip rate vertical component (mm/yr)	Average recurrence interval (yrs)
814	814-2-1	Koshiki FZ	Koshiki segment (North-eastern part)	129.994	31.793	2	12	12	96.1	60	–	N (+LL)	−12.15	LL	N	–	0.3–1.0	2400–11000
814	814-2-2	Koshiki FZ	Koshiki segment (South-western part)	129.749	31.622	2	30	18	50.6	50	SE	N	−119.73	N	Y	–		
815	815	Hijiu FZ		131.133	33.310	3	46	14	84.5	70	S	N	−87.36	N	Y	–	0.1–0.2	20,000–27000
816	816	Haneyama-Kuenohi-rayama FZ		130.964	33.235	3	36	14	101.5	70	S	N	−47.11	N	Y	–	–	2100–3700
817	817	Kokura-higashi F		130.894	34.003	3	28	14	186.5	70	W	RL (+R)	157.66	RL	Y	–	(≤) 0.03–0.1	–
818	818-1	Ichiki FZ	Ichiki segment	130.112	31.726	2	30	14	90.4	60	S	N (+RL)	−12.34	LL	N	–	–	–
818	818-2	Ichiki FZ	Koshiki-kaikyo central segment	129.922	31.451	2	42	12	31.5	75	SE	N	172.96	RL	N	–	–	–
818	818-3	Ichiki FZ	Fukiage-hama seiho-oki segment	130.310	31.646	2	24	12	223	75	NW	N	−121.42	N	Y	–	–	–

The parameters of the fault models are according to the J-SHIS by NIED

[a] *R* reverse, *N* normal, *RL* right-lateral, *LL* left-lateral

Concluding remarks and future development

The method of estimating realistic rake angles from a 3D tectonic stress field according to WBH was validated by comparison to focal mechanism data. The calculated rake angles accurately reproduced the observed rake angles; λ, the misfit angles between the observed and calculated rake angles, mostly ranged between $-30°$ and 30°. During Period I (January 1997 to January 2007), the absolute misfit angles, $|\lambda|$, were $\leq 30°$ for approximately 94.4% (for all M_w) and 86.2% (for $M_w \geq 6.0$) of earthquakes. $|\lambda|$ values were $\leq 30°$ for approximately 75.1% (for all M_w) and 91.7% (for $M_w \geq 6.0$) of earthquakes in Period II (February 2007 to the occurrence time of the 2011 Tohoku-oki earthquake). After the occurrence of the 2011 Tohoku-oki earthquake (Period III), large $|\lambda|$ values were typically observed in the source and neighboring regions of the 2011 Tohoku-oki earthquake, whereas the calculated rake angles were mostly consistent with the observed rake angles as similar to periods I and II. Considering that the uncertainties of focal mechanism solutions generally range from 20 to 30° (e.g., Ishibe et al. 2014), our study supports the applicability of the WBH method for evaluating the expected rake angles of future large earthquakes from seismologically estimated tectonic stress fields. The $|\lambda|$ values were large for the focal mechanism solutions of earthquakes in the source and nearby the occurrences of large earthquakes such as the 2011 Tohoku-oki earthquake (e.g., Fig. 12), the seismically inactive areas where the number of available mechanism data to invert the stress is limited (e.g., prefectural boundary region between Ibaraki and Fukushima, Fig. 14), and/or far offshore areas where the observation stations are sparsely distributed. Our study also elucidates the necessity of paying close attention to apply the method to the above areas.

We suggested four possible causes for generating a large $|\lambda|$. The coseismic (and postseismic) stress changes imparted by major earthquakes such as the 2011 Tohoku-oki earthquake can change the stress pattern and generate a large $|\lambda|$. One representative example is the off Fukushima and Ibaraki region, the southern margin of the main rupture area of the 2011 Tohoku-oki earthquake (Terakawa and Matsu'ura 2023). The incomplete understanding of the tectonic stress field because of a lack of available data for short-term periods is also a possible factor for generating a large $|\lambda|$. The distribution of focal mechanism solutions of earthquakes used for the CMT data inversion is spatially heterogeneous, and available mechanism data are very limited in several regions, such as the prefectural boundary region between Ibaraki and Fukushima. The local heterogeneity of the stress field that deviates from the regional stress field and the activation of seismicity in such regions would generate a large $|\lambda|$. Local deviatoric stress changes caused by the pore-fluid pressure increase enforced by the intrusion of high-pressure fluid into a fault zone (Matsu'ura and Terakawa 2021) and the presence of large uncertainties in focal mechanism solutions for earthquakes (e.g., comparatively low VR along the Izu–Bonin Trench and Ryukyu Trench) are other possible factors generating a large $|\lambda|$.

In the present study, we also confirmed that the fault types obtained from the 3D tectonic stress field with WBH coincided well with the geomorphologically and geologically estimated fault types for FZs in Kyushu district, southwest Japan. In the Futagawa and Hinagu FZs, large earthquakes called the 2016 Kumamoto earthquake sequence occurred in April 2016. The rake angles calculated from the WBH method were consistent with both geomorphologically and geologically estimated fault types and observed rake angles. These results suggest that the rake angles for faults with known geometry can be accurately derived from the 3D tectonic stress field with WBH, whereas there are limitations for applying this method to a region where the stress has been perturbed due to recent large earthquakes (e.g., the 2011 Tohoku-oki earthquake) and/or a region where the uncertainty of stress orientations is large, for example, due to a limited number of available focal mechanisms and sparse distribution of observation stations. A comprehensive study for Quaternary active faults in Japan by comparing calculated rake angles from tectonic stress fields according to WBH with geomorphologically and geologically evaluated fault types would be helpful for further understanding the temporal stability of tectonic stress fields from seismological data for ~10 years and the availability of the tectonic stress field with WBH to constrain the fault slip directions for future large earthquakes.

Why the tectonic stress field obtained from the CMT data inversion is consistent with the WBH? The moment tensor of a seismic event is mathematically equivalent to the volume integral of coseismic static stress changes over the whole region surrounding the source (Matsu'ura et al. 2019). Based on this relationship, in the CMT data inversion method, they represent the CMT data of a seismic event by the weighted volume integral of the stress field (Terakawa and Matsu'ura 2008, 2023). This formulation is attributed to the idea that seismic events release a part of the stress field, or that seismic events whose moment tensors are consistent with the stress tensor are the most likely. Meanwhile, based on the volume integral representation of the moment tensor, Matsu'ura et al. (2019) further elucidated that seismic slip in the direction of the resolved shear stress maximizes the efficiency of elastic strain energy release under realistic stress conditions. Therefore, WBH assumes that seismic slip occurs (in

the direction of the resolved shear stress) at preexisting faults to release elastic strain energies most effectively. A seismic event can release elastic strain energies most effectively when its moment tensor is consistent with the stress tensor (Matsu'ura and Terakawa 2021). Thus, the formulation of the CMT data inversion method as above is supported by the same assumption as the WBH. In other words, the most likely seismic slip is a physical process that releases elastic strain energy most effectively. It is very interesting that the results of the present study substantiate these physical backgrounds of the CMT data inversion and WBH.

The current method for predicting strong ground motion ("Recipe") by HERP (HERP 2020) is based on the characterized source model consisting of several asperities with large slip amounts and background regions with smaller slip amounts (e.g., Irikura and Miyake 2011). The Recipe recommends setting rake angles as 90° for reverse faults, −90° for normal faults, 0° for left-lateral faults, and 180° for right-lateral faults for active faults for which the rake angle is not specified by the subcommittee of the long-term evaluation. However, the effect of rake angle on tsunami forecasting is not negligible (Satake et al. 2022), and it is worth discussing utilizing rake angles expected from the tectonic stress field with WBH for forecasting strong ground motions and tsunamis. There are several issues in evaluating strong ground motions and/or tsunamis that contribute to disaster prevention and mitigation. Seismicity is spatially and temporally heterogeneous, and the uncertainty of the estimated 3D tectonic stress field depends on the seismicity. Evaluating the uncertainties of the rake angles arising from the uncertainties of the stress field is therefore an important issue (e.g., Terakawa 2017). Information on fault geometry (fault location, strike, and dip angle) is also essential to calculate rake angles expected from tectonic stress fields with WBH, and the improvement of fault imaging techniques and data accumulation through additional surveys are also important issues to improve the reliability of strong ground motion and/or tsunami predictions.

Abbreviations

3D	Three-dimensional
CMT	Centroid moment tensor
ERC	Earthquake Research Committee
FZ(s)	Fault zone(s)
FS(s)	Fault segment(s)
HERP	Headquarters for Earthquake Research Promotion
JUNEC FM^2	Japan University Network Earthquake Catalog of First-Motion Focal Mechanisms
TM2010	Terakawa and Matsu'ura (2010)
WBH	Wallace–Bott hypothesis
λ	Misfit angle between the observed and calculated rake angles
$\|\lambda\|$	Absolute misfit angle between the observed and calculated rake angles

Supplementary Information

The online version contains supplementary material available at https://doi.org/10.1186/s40623-023-01955-9.

Additional file 1: Figure S1. Distribution of focal mechanism solutions from the Japan University Network Earthquake Catalog First-Motion Focal Mechanism (JUNEC FM^2; Ishibe et al. 2014). The color of the focal sphere shows the fault type according to the criteria by Frohlich (1992).

Additional file 2: Figure S2. Distribution of focal mechanism solutions with calculated rake angles for JUNEC FM^2.

Additional file 3: Figure S3. Misfit angles between the observed and calculated rake angles for JUNEC FM^2.

Additional file 4: Figure S4. Occurrence times of earthquakes vs. λ for JUNEC FM^2.

Additional file 5: Figure S5. Close-up figure of (a) F-net focal mechanism solutions (left) and focal mechanism solutions with calculated rake angles (right) in the Hokkaido district during period I. The colors of the focal sphere indicate the fault types according to the classification criteria by Frohlich (1992). (b) Distribution of λ.

Additional file 6: Figure S6. Those in the Hokkaido district during period II. The symbols are the same as in Fig. S5.

Additional file 7: Figure S7. Those in the Hokkaido district during period III. The symbols are the same as in Fig. S5.

Additional file 8: Figure S8. Those in the Tohoku district during period I. The symbols are the same as in Fig. S5.

Additional file 9: Figure S9. Those in the Tohoku district during period II. The symbols are the same as in Fig. S5.

Additional file 10: Figure S10. Those in the Tohoku district during period III. The symbols are the same as in Fig. S5.

Additional file 11: Figure S11. Those in the Kanto and Chubu districts during period I. The symbols are the same as in Fig. S5.

Additional file 12: Figure S12. Those in the Kanto and Chubu districts during period II. The symbols are the same as in Fig. S5.

Additional file 13: Figure S13. Those in the Kanto and Chubu districts during period III. The symbols are the same as in Fig. S5.

Additional file 14: Figure S14. Those in the Chugoku and Shikoku districts during period I. The symbols are the same as in Fig. S5.

Additional file 15: Figure S15. Those in the Chugoku and Shikoku districts during period II. The symbols are the same as in Fig. S5.

Additional file 16: Figure S16. Those in the Chugoku and Shikoku districts during period III. The symbols are the same as in Fig. S5.

Additional file 17: Figure S17. Those in the Kyushu district during period I. The symbols are the same as in Fig. S5.

Additional file 18: Figure S18. Those in the Kyushu district during period II. The symbols are the same as in Fig. S5.

Additional file 19: Figure S19. Those in the Kyushu district during period III. The symbols are the same as in Fig. S5.

Additional file 20: Figure S20. Those in the Ryukyu Trench region during period I. The symbols are the same as in Fig. S5.

Additional file 21: Figure S21. Those in the Ryukyu Trench region during period II. The symbols are the same as in Fig. S5.

Additional file 22: Figure S22. Those in the Ryukyu Trench region during period III. The symbols are the same as in Fig. S5.

Additional file 23: Figure S23. Those in the Izu–Bonin Trench region during period I. The symbols are the same in Fig. S5.

Additional file 24: Figure S24. Those in the Izu–Bonin Trench region during period II. The symbols are the same as in Fig. S5.

Additional file 25: Figure S25. Those in the Izu–Bonin Trench region during period III. The symbols are the same as in Fig. S5.

Additional file 26: Figure S26. Distribution of variance reductions (VR) for the F-net mechanism solutions for (a) period I, (b) period II, and (c) period III.

Acknowledgements
We would like to thank an associate editor Prof. Yohei Yukutake and two anonymous reviewers for their helpful comments. We used the F-net focal mechanism solutions of earthquakes (https://doi.org/10.17598/nied.0005) provided by the National Research Institute for Earth Science and Disaster Resilience and the fault models for major active fault zones by the Japan Seismic Hazard Information Station (J-SHIS: https://www.j-shis.bosai.go.jp/en/). We also used the Generic Mapping Tools (Wessel and Smith 1998) for drawing the figures. We thank all the organizations and individuals who provided data and information used in this study.

Author contributions
TI performed numerical and statistical analyses and drafted the manuscript. TT and AH contributed to the data preparation and numerical analyses, contributed to the interpretation of the results, and wrote the manuscript. MM and RSM led the research and contributed to interpreting the results and writing the manuscript.

Funding
This study has been supported by the Headquarters for Earthquake Research Promotion (HERP) of the Ministry of Education, Culture, Sports, Science, and Technology (MEXT) of Japan.

Availability of data and materials
JUNEC can be obtained from the Earthquake Research Institute (ERI) FTP site, ftp://ftp.eri.u-tokyo.ac.jp/pub/data/junec/hypo/ (last accessed June 2022). JUNEC FM^2 is available at ftp://ftp.eri.u-tokyo.ac.jp/pub/data/junec/mech/ (last accessed June 2022). Focal mechanism solutions for earthquakes were provided by the National Research Institute for Earth Science and Disaster Resilience (https://www.fnet.bosai.go.jp/event/search.php?LANG=en, last accessed March 2023).

Declarations

Ethics approval and consent to participate
Not applicable.

Consent for publication
Not applicable.

Competing interests
The authors declare that they have no competing interests.

Author details
[1]Association for the Development of Earthquake Prediction, Chiyoda Build. 8F, 1-5-18, Kanda-Sarugakucho, Chiyoda, Tokyo 101-0064, Japan. [2]The Institute of Statistical Mathematics, Tachikawa, Japan. [3]Nagoya University, Nagoya, Japan. [4]Tokyo Gakugei University, Koganei, Japan. [5]National Research Institute for Earth Science and Disaster Resilience, Tsukuba, Japan.

Received: 7 July 2023 Accepted: 15 December 2023
Published online: 06 February 2024

References

Akaike H (1980) Likelihood and the Bayes procedure. In: Bernardo JM et al (eds) Bayesian statistics. Valencia Univ. Press, Valencia, pp 143–166
Annaka T, Satake K, Sakakiyama T, Yanagisawa K, Shuto N (2007) Logic-tree approach for probabilistic tsunami hazard analysis and its applications to the Japanese coasts. Pure Appl Geophys 164:577–592
Aoi S, Asano Y, Kunugi T, Kimura T, Uehira K, Takahashi N, Ueda H, Shiomi K, Matsumoto T, Fujiwara H (2020) MOWLAS: NIED observation network for earthquake, tsunami and volcano. Earth Planets Space 72:126. https://doi.org/10.1186/s40623-020-01250-x
Baba T, Hori T (2006) Heterogeneous interplate coupling in the southern Kuril subduction zone inferred from back slip inversion analysis with the minimum solution norm constraint, Eos Trans AGU, West. Pac. Geophys. Meet. Suppl., Abstract T12A–04. 87(36)
Bott MHP (1959) The mechanics of oblique slip faulting. Geol Mag 96(2):109–117
Frohlich C (1992) Triangle diagrams: ternary graphs to display similarity and diversity of earthquake focal mechanisms. Phys Earth Planet Inter 75:193–198
Gephart JW, Forsyth DW (1984) An improved method for determining the regional stress tensor using earthquake focal mechanism data: application to the San Fernando earthquake sequence. J Geophys Res Solid Earth 89:9305–9320
Headquarters for Earthquake Research Promotion (HERP) (2013) Regional evaluation of active faults in Kyushu district, 81pp
Headquarters for Earthquake Research Promotion (HERP) (2020) Strong ground motion prediction method for earthquakes with specified source faults ("Recipe") (as of 2020 March 6th). 53pp
Hirose F, Miyaoka K, Hayashimoto N, Yamazaki T, Nakamura M (2011) Outline of the 2011 off the Pacific coast of Tohoku earthquake (Mw 9.0)—seismicity: foreshocks, mainshock, aftershocks, and induced activity. Earth Planets Space 63:513–518. https://doi.org/10.5047/eps.2011.05.019
Huzita K (1980) Role of the median tectonic line in the Quaternary tectonics of the Japanese islands. Mem Geol Soc Jpn 18:129–153
Imanishi K, Kuwahara Y (2009) Stress field in the source region after the 2007 Mw6.6 Niigataken Chuetsu-oki earthquake deduced from aftershock focal mechanisms: implication for a pre-mainshock stress field. Earth Planets Space 61:1053–1065. https://doi.org/10.1186/BF03352956
Imanishi K, Ando R, Kuwahara Y (2012) Unusual shallow normal-faulting earthquake sequence in compressional northeast Japan activated after the 2011 off the Pacific coast of Tohoku earthquake. Geophys Res Lett 39:L09306. https://doi.org/10.1029/2012GL051491
Irikura K, Miyake H (2001) Prediction of strong ground motions for scenario earthquakes. J Geogr 110(6):849–875 (**in Japanese with English abstract**)
Irikura K, Miyake H (2011) Recipe for predicting strong ground motion from crustal earthquake scenarios. Pure Appl Geophys 168(1–2):85–104
Ishibe T, Shimazaki K (2008) The Gutenberg–Richter relationship vs. the characteristic earthquake model: effects of different sampling methods. Bull Earthq Res Inst Univ Tokyo 83:131–151
Ishibe T, Shimazaki K (2009) Seismicity in a source region of a large interplate earthquake and the characteristic earthquake model. Earth Planets Space 61:1041–1052. https://doi.org/10.1186/BF03352955
Ishibe T, Shimazaki K (2012) Characteristic earthquake model and seismicity around Late Quaternary active faults in Japan. Bull Seismol Soc Am 102:1041–1058
Ishibe T, Shimazaki K, Satake K, Tsuruoka H (2011a) Change in seismicity beneath the Tokyo metropolitan area due to the 2011 off the Pacific coast of Tohoku, Japan Earthquake. Earth Planets Space 63:731–735. https://doi.org/10.5047/eps.2011.06.001
Ishibe T, Shimazaki K, Tsuruoka H, Yamanaka Y, Satake K (2011b) Correlation between Coulomb stress changes imparted by large historical strike-slip earthquakes and current seismicity in Japan. Earth Planets Space 63:301–314. https://doi.org/10.5047/eps.2011.01.008
Ishibe T, Tsuruoka H, Satake K, Nakatani M (2014) A focal mechanism solution catalog of earthquakes (M≥2.0) in and around the Japanese Islands for 1985–1998. Bull Seismol Soc Am 104:1031–1036. https://doi.org/10.1785/0120130278
Ishibe T, Satake K, Sakai S, Shimazaki K, Tsuruoka H, Yokota Y, Nakagawa S, Hirata N (2015) Correlation between Coulomb stress imparted by the 2011 Tohoku-Oki earthquake and seismicity rate change in Kanto, Japan. Geophys J Int 201:112–134. https://doi.org/10.1093/gji/ggv001
Ishibe T, Ogata Y, Tsuruoka H, Satake K (2017) Testing the Coulomb stress triggering hypothesis for three recent megathrust earthquakes. Geosci Lett 4:5. https://doi.org/10.1186/s40562-017-0070-y
Iwata T, Sekiguchi H, Asano K, Ohori M, Kagawa T, Noguchi T, Yamanaka H, Chimoto K, Miyake H, Fujiwara H, Morikawa N, Horikawa H (2018) Evaluation of strong ground motion. In: Annual progress reports of the integrated

research project on seismic and tsunami hazards around the Sea of Japan (in the fiscal year of 2017), pp 353–439 (**in Japanese**)
Kato A, Sakai S, Obara K (2011) A normal-faulting seismic sequence triggered by the 2011 off the Pacific coast of Tohoku earthquake: wholesale stress regime changes in the upper plate. Earth Planets Space 63(7):745–748. https://doi.org/10.5047/eps.2011.06.014
Katsumata K (2011) Precursory seismic quiescence before the *Mw* = 83 Tokachi-oki, Japan, earthquake on 26 September 2003 revealed by a re-examined earthquake catalog. J Geophys Res Solid Earth 116:B10307. https://doi.org/10.1029/2010JB007964
King GCP, Stein RS, Lin J (1994) Static stress changes and the triggering of earthquakes. Bull Seismol Soc Am 84:935–953
Matsumoto S, Yamashita Y, Nakamoto M, Miyazaki M, Sakai S, Iio Y, Shimizu H, Goto K, Okada T, Ohzono M, Terakawa T, Kosuga M, Yoshimi M, Asano Y (2018) Prestate of stress and fault behavior during the 2016 Kumamoto earthquake (M7.3). Geophys Res Lett 45(2):637–645
Matsushita R, Imanishi K (2015) Stress fields in and around metropolitan Osaka, Japan, deduced from microearthquake focal mechanisms. Tectonophysics 642:46–57
Matsu'ura M, Terakawa T (2021) Decomposition of elastic potential energy and a rational metric for aftershock generation. Geophys J Int 227(1):162–168
Matsu'ura M, Noda A, Terakawa T (2019) Physical interpretation of moment tensor and the energetics of shear faulting. Tectonophysics 771:228228
Michael AJ (1984) Determination of stress from slip data: faults and folds. J Geophys Res Solid Earth 89:11517–11526
Michael AJ (1987) Use of focal mechanisms to determine stress: a control study. J Geophys Res Solid Earth 92:357–368
Mulia IE, Ishibe T, Satake K, Gusman AR, Murotani S (2020) Regional probabilistic tsunami hazard assessment associated with active faults along the eastern margin of the Sea of Japan. Earth Planets Space 72:123. https://doi.org/10.1186/s40623-020-01256-5
Murotani S, Satake K, Fujii Y (2013) Scaling relations of seismic moment, rupture area, average slip, and asperity size for M~9 subduction-zone earthquakes. Geophys Res Lett 40(19):5070–5074
Murotani S, Matsushima S, Azuma T, Irikura K, Kitagawa S (2015) Scaling relations of source parameters of earthquakes occurring on inland crustal mega-fault systems. Pure Appl Geophys 172(5):1371–1381
Murotani S, Satake K, Ishibe T, Harada T (2022) Reexamination of tsunami source models for post 20th century earthquakes off-Hokkaido and off-Tohoku in the eastern margin of the Sea of Japan. Earth Planets Space 74:52. https://doi.org/10.1186/s40623-022-01607-4
National Research Institute for Earth Science and Disaster Resilience (2023) NIED F-net. National Research Institute for Earth Science and Disaster Resilience. https://doi.org/10.17598/NIED.0005
Nishimura S, Hashimoto M, Ando M (2004) A rigid block rotation model for the GPS derived velocity field along the Ryukyu arc. Phys Earth Planet Inter 142:185–203. https://doi.org/10.1016/j.pepi.2003.12.014
Ogata Y (2005) Synchronous seismicity changes in and around the northern Japan preceding the 2003 Tokachi-oki earthquake of M8.0. J Geophys Res Solid Earth 110:B08305. https://doi.org/10.1029/2004JB003323
Okada Y, Kasahara K, Hori S, Obara K, Sekiguchi S, Fujiwara H, Yamamoto A (2004) Recent progress of seismic observation networks in Japan—Hi-net, F-net, K-NET and KiK-net. Earth Planets Space 56:xv–xxviii. https://doi.org/10.1186/BF03353076
Research Committee on Large Earthquakes in the Sea of Japan (2014) Report of the Research Committee on Large Earthquakes in the Sea of Japan. 470pp. http://www.mlit.go.jp/river/shinngikai_blog/daikibojishinchousa/
Satake K, Ishibe T, Murotani S, Mulia IE, Gusman AR (2022) Effect of uncertainty in fault parameters on deterministic tsunami simulation: example for active faults along the eastern margin of the Sea of Japan. Earth Planets Space 74:36. https://doi.org/10.1186/s40623-022-01594-6
Somerville PG, Irikura K, Graves R, Sawada S, Wald D, Abrahamson N, Iwasaki Y, Kagawa T, Smith N, Kowada A (1999) Characterizing crustal earthquake slip models for the prediction of strong ground motion. Seismol Res Lett 70:59–80
Stein RS, King GCP, Lin J (1992) Change in failure stress on the southern San Andreas fault system caused by the 1992 Magnitude=7.4 Landers earthquake. Science 258:1328–1332
Takeda T, Asano Y, Shiomi K, Matsumoto T, Kimura H, Matsuzawa K, Ueno T, Kimura T (2014) Seismicity analysis in the Japan Sea coastal regions. In: Annual progress reports of the integrated research project on seismic and tsunami hazards around the Sea of Japan (in the fiscal year of 2013), pp 217–232 (**in Japanese**)
Takemura M (1998) Scaling law for Japanese intraplate earthquakes in special relations to the surface faults and the Damages. Zisin J Seismol Soc Jpn Ser 51(2):211–228 (**in Japanese with English abstract**)
Terakawa T (2017) Overpressurized fluids drive microseismic swarm activity around Mt. Ontake volcano, Japan. Earth Planets Space 69:87. https://doi.org/10.1186/s40623-017-0671-x
Terakawa T, Matsu'ura M (2008) CMT data inversion using a Bayesian information criterion to estimate seismogenic stress fields. Geophys J Int 172:674–685. https://doi.org/10.1111/j.1365-246X.2007.03656.x
Terakawa T, Matsu'ura M (2010) The 3-D tectonic stress fields in and around Japan inverted from centroid moment tensor data of seismic events. Tectonics 29:TC6008. https://doi.org/10.1029/2009TC002626
Terakawa T, Matsu'ura M (2023) Tectonic stress fields inferred from long-term CMT data ranging over different periods. Geophys J Int 233:162–181
Terakawa T, Hashimoto C, Matsu'ura M (2013) Changes in seismic activity following the 2011 Tohoku-oki earthquake: effects of pore fluid pressure. Earth Planet Sci Lett 365:17–24
Toda S, Stein RS, Reasenberg PA, Dieterich JH, Yoshida A (1998) Stress transferred by the 1995 Mw= 6.9 Kobe, Japan, shock: effect on aftershocks and future earthquake probabilities. J Geophys Res Solid Earth 103(B10):24543–24565
Toda S, Stein RS, Lin J (2011) Widespread seismicity excitation throughout central Japan following the 2011 M=9.0 Tohoku earthquake and its interpretation by Coulomb stress transfer. Geophys Res Lett 38:L00G03. https://doi.org/10.1029/2011GL047834
Uchide T, Shiina T, Imanishi K (2022) Stress map of Japan: detailed nationwide crustal stress field inferred from focal mechanism solutions of numerous microearthquakes. J Geophys Res Solid Earth 127:e2022JB024036
Wallace RE (1951) Geometry of shearing stress and relation to faulting. J Geol 59(2):118–130
Wells DL, Coppersmith KJ (1994) New empirical relationships among magnitude, rupture length, rupture width, rupture area, and surface displacement. Bull Seismol Soc Am 84(4):974–1002
Wesnousky SG, Scholz CH, Shimazaki K (1982) Deformation of island arc: rates of moment release and crustal shortening in intraplate Japan determined from seismicity and Quaternary fault data. J Geophys Res 87:6829–6852. https://doi.org/10.1029/JB087iB08p06829
Wessel P, Smith WHF (1998) New, improved version of generic mapping tools released. EOS Trans AGU 79(47):579
Yamada M, Ohmura J, Goto H (2017) Wooden building damage analysis in Mashiki Town for the 2016 Kumamoto earthquakes on April 14 and 16. Earthq Spectra 33:1555–1572
Yoshii T (1979) A detailed cross-section of the deep seismic zone beneath northeastern Honsyu, Japan. Tectonophysics 55:349–360. https://doi.org/10.1016/0040-1951(79)90183-5

Publisher's Note